

Validation of the Aura MLS Cloud Ice Water Content (IWC) Measurements

5 Dong L. Wu¹, Jonathan H. Jiang¹, William G. Read¹, Richard T. Austin², Cory P. Davis³,
Alyn Lambert¹, Brian H. Kahn¹, Christopher J. Nankervis³, Maarten Snee⁴, J. Pepijn Veefkind⁴,
Hugh C. Pumphrey³, Graeme L. Stephens², Deborah G. Vane¹, and Joe W. Waters¹

1. Jet Propulsion Laboratory, California Institute of Technology, Pasadena, California, USA.
- 10 2. Department of Atmospheric Science, Colorado State University, Fort Collins, Colorado, USA.
3. Institute of Atmospheric and Environmental Science, School of GeoSciences, University of Edinburgh, Edinburgh, Scotland, UK.
- 15 4. Climate Research and Seismology Department, Royal Netherlands Meteorological Institute (KNMI), De Bilt, Netherlands.

Version: Final

Date: May 7, 2007

20 To be submitted to: Journal of Geophysical Research – Atmosphere
(Aura special issue)

Abstract – Retrieval and validation of upper-tropospheric ice water content (IWC) measurements with the Aura Microwave Limb Sounder (MLS) are described. The MLS version 2.2 (V2.2) IWC, derived from 240-GHz cloud-induced radiances (T_{cir}) at high tangent heights, is scientifically useful at 215-83 hPa. The V2.2 IWC represents a bulk cloud property averaged over a $\sim 300 \times 7 \times 4 \text{ km}^3$ volume near the pointing tangent height. Precision, accuracy and spatial resolution of the V2.2 IWC are determined through model simulations and comparisons with other correlative datasets. Comparisons with AIRS (Atmosphere Infrared Sounder), OMI (Ozone Monitoring Instrument) and MODIS (Moderate Resolution Imaging Spectroradiometer) indicate that MLS cloud top heights are higher than those measurements by $\sim 1.5 \text{ km}$. Comparisons of MLS V2.2 and CloudSat IWCs are made in terms of normalized probability density function (PDF) for months of January and July. The differences between MLS and CloudSat IWC PDFs are generally less than 50%. At pressures $< 177 \text{ hPa}$ and extratropical latitudes, the MLS V2.2 IWC exhibits a slightly low bias compared to CloudSat, part of which can be attributed to MLS retrieval systematic errors. Cloud inhomogeneity and particle size distribution (PSD) are the largest contributors to V2.2 IWC uncertainties.

1 Introduction

Clouds are a major source of uncertainty in understanding climate variability (Houghton et al., 2001). Reducing the cloud uncertainty requires more observations than just cloud fraction and cloud top height that have been obtained to date from space. Global observations of ice water content (IWC), a key parameter that determines cloud radiative and hydrological properties, remain lacking partly because of complicated microphysics in ice clouds (e.g., Comstock et al., 2007). Lack of guidance from observations leads to poor-fidelity predictions of cloud feedbacks in a changing climate.

Remote sensing of cloud ice with passive mm and sub-mm wave radiometry offers great potential for obtaining global cloud ice amounts needed by climate and weather research. Recently, several studies have been made on microwave sensors for retrieving cloud ice water path (IWP) [e.g., Vivekanandan et al., 1991; Gasiewski, 1992; Evans and Stephens, 1995; Evans et al., 1998; Liu and Curry, 2000; Weng and Grody, 2000; Skofronick-Jackson and Wang, 2000; Eriksson et al., 2007]. Unlike visible/IR techniques, microwave radiation can penetrate into dense clouds and interact with ice particles to measure ice mass and other bulk properties like IWC and effective radius of ice crystals [Evans et al., 2005].

As a relatively new remote sensing technique, MLS (Microwave Limb Sounder) can measure cloud ice in the upper troposphere with limb millimeter and submillimeter wave radiometry. [Waters et al., 1993; Wu and Jiang, 2004; Wu et al., 2005; Waters et al., 2006]. In addition to the advantages associated with nadir-viewing microwave sensors, MLS can measure upper-tropospheric clouds, which does not require knowledge of atmospheric temperature lapse rate (as in the nadir case) and is not significantly affected by surface properties. In a previous study, Wu et al. [2005] made the first global IWC observations near the tropopause using MLS 203 GHz

measurements from UARS (Upper Atmosphere Research Satellite) in 1991-1997. The UARS MLS study demonstrated that cloud features observed by microwaves can provide quantitative information on cloud ice amount in the upper troposphere, which has important implications for H₂O transport and dehydration in that region.

5 Aura MLS was launched in July 2004 and has seven radiometers with frequencies near 118 (H,V), 190(V), 240(H), 640(H) GHz and 2.5 (H,V) THz for horizontal (H) and vertical (V) polarizations. All the MLS radiometers can detect cloud-induced radiance changes [Wu et al., 2006]. Since the initial release of version 1.5 (V1.5) products in 2004, the MLS team has improved the level 2 algorithm and released version 2.2 (V2.2) products in 2006. The V2.2 IWC
10 is retrieved from the 240 GHz measurements at high tangent heights where the radiances can penetrate through atmospheric limb.

Analyses of the initially released V1.5 cloud data revealed some serious shortfalls of global general circulation models (GCMs) in cloud parameterization and predictability [J.-L. Li et al., 2005; Li et al., 2007]. The MLS cloud data have also been used to study tropical super
15 greenhouse effects [Su et al., 2006] and roles of convective lifting in pollution transport [Q. B. Li et al., 2005; Fu et al., 2006]. In addition to cloud ice, Aura MLS also measures upper tropospheric temperature (*T*), H₂O, CO, O₃, and HNO₃ profiles, together providing a comprehensive view of deep convection, hydrological cycle, and transport in this region [Schwartz et al., 2007; Read et al., 2007; Livesey et al., 2007; Jiang et al., 2007; Santee et al.,
20 2007]. Aura is part of the NASA A-Train and flies in formation with Aqua, CloudSat and CALIPSO (Cloud-Aerosol Lidar and Infrared Pathfinder Satellite Observation), creating a large ensemble of closely-sampled cloud data and an unprecedented opportunity for quantifying/improving accuracy of global cloud ice measurements.

The aim of this paper is to assess accuracy, precision, and resolution of the MLS V2.2 IWC measurement through model simulations and comparisons with other correlative datasets. The rest of the paper is organized to have the MLS IWC retrieval described in section 2, including retrieval models, spatial resolution and data usage. Section 3 provides MLS IWC precision and uncertainty estimates. Comparisons with AIRS (Atmosphere Infrared Sounder), OMI (Ozone Monitoring Instrument) and MODIS (Moderate Resolution Imaging Spectroradiometer) are given in section 4, and comparisons with CloudSat in section 5. Finally, conclusions and future work are presented in section 6.

2 Aura MLS IWC Measurements

2.1 Limb Radiances and Cloud Handling

The Aura satellite has a 705-km sun-synchronous ($\sim 1:40$ p.m. ascending crossing time) orbit with 98° inclination. MLS limb scans are synchronized to the orbital period with 240 limb scans (called the major frames or MAFs) per orbit in the nominal operation. MLS latitude coverage is from 82°S to 82°N with the tangent track close to the Aqua nadir footprint but ~ 8 min behind. Unlike the step-and-stare scans used by UARS MLS, Aura MLS scans are continuous in tangent height (h_t) from the surface to ~ 92 km in 24.7s. The data integration time for each measurement is 1/6 second, called a minor frame (MIF). For the GHz measurements, each MAF or scan has 40-50 MIFs useful for tropospheric cloud observations with a 300 m sampling resolution in tangent height. More on the MLS operation, onboard calibration, and radiance noise can be found in Jarnot et al. [2006].

Except for the 118 GHz, all MLS radiometers are double-sideband receivers, meaning that the measured radiance is a sum of radiation from two sideband frequencies (separated in frequency by 4-40 GHz). The Aura MLS antenna views forward in the satellite flying direction. Its cross-

track FOVs (field-of-view) are respectively 12, 8.4, 6.4, 2.9, and 2.1 km at 118, 190, 240, 640 GHz and 2.5 THz, and the corresponding vertical FOVs are 5.8, 4.2, 3.2, 1.4, and 2.1 km [Cofield and Stek, 2006; Pickett 2006].

MLS cloud flags and cloud ice retrievals are made from radiance measurements in the window channels that are least affected by clear-sky atmospheric absorption in each radiometer and can penetrate to a lower altitude than other channels. MLS radiances can be affected by clouds when the pointing is near or below cloud top. The fundamental quantity for MLS cloud measurements is the *cloud-induced radiance* (T_{cir}), which is defined as the difference between the measured radiance and the expected clear-sky radiances at each tangent pressure (P_{tan}). In the MLS V2.2 algorithm, the expected clear-sky radiance is calculated with the radiative transfer (RT) model in the Level 2 retrieval [Read et al., 2006], using the retrieved atmospheric state as input.

Clouds can induce a positive or negative T_{cir} depending on the background limb radiance and scattering properties of ice particles. T_{cir} must be greater than uncertainties of the measured and modeled radiances in order to be qualified as a cloud. T_{cir} is generally spectrally flat within MLS radiometer bandwidth (a few GHz). However, where cloud scattering is strong, MLS radiance spectra may differ substantially from the clear-sky ones and result in frequency-dependent T_{cir} in a narrow spectral band. This is because interacting with radiation from different directions in strong cloud scattering cases can alter the observed spectral shapes of emission gas molecules (e.g., O_2 , H_2O , O_3) and cause artifacts in MLS gas retrievals. Because the V2.2 forward model does not include cloud scattering effects [Read et al., 2006], the retrieval algorithm for gases and temperature needs to exclude the limb radiances associated with large

Tcir. For those affected by small *Tcir*, the V2.2 retrieval algorithm can handle cloud effects by retrieving a radiance-additive baseline or extinction profile.

As in MLS V1.5 data processing [Livesey et al., 2006], the V2.2 algorithm is designed to retrieve atmospheric gas profiles and *Tcir* through multiple phases (Appendix A). As the retrieval progresses through its phase, accuracies of the retrieved *Tcir* and clear-sky atmospheric profiles are improved together in an iterative sense. In MLS Level 2 processing, *Tcir* is also used to flag radiance measurements for possible cloud contamination so that the algorithm can treat them differently. The retrieved *Tcir* for clear sky situations are normally within their noise, and we set an upper and a lower bound to flag outliers as possibly strong cloud scattering for each radiometer (Appendix A). *Tcir* is usually computed at the end of a retrieval phase in preparation for the next retrieval phase. As an exception, the R3 (240 GHz) cloud flag is based on the chi-square (χ^2) value of band 8 radiances (233.9 GHz O¹⁸O line), which is obtained from the radiance fit of the entire band in the end of the *Core* phase (Appendix A). The *Tcir* calculation is finalized in the *HighCloud* phase for all MLS radiometers (see Appendix A) after the key atmospheric profiles (*T*, *Ptan*, H₂O, O₃, HNO₃) have been retrieved. The IWC retrieval uses the final 240-GHz *Tcir* that is derived as follows. The radiative transfer (RT) model computes the expected clear-sky radiances using the best atmospheric state retrieved before *HighCloud* phase. In addition, the retrieved H₂O is capped such as the corresponding relative humidity with respect to ice (*RHi*) does not exceed 110%. This constraint helps to eliminate occasional *Tcir* spikes from the H₂O retrieval, but may induce extra error from the *T* retrieval. The difference between the measured and the modeled radiances gives the final *Tcir*. The *Tcir*'s derived from each retrieval phase are stored in the Level 2 auxiliary file for clouds (L2AUX-Cloud).

2.2 Cloudy-Sky Radiative Transfer (RT) Models

One-Dimensional (1-D) Model

For cloud IWC retrieval, we developed a 1-D RT model to compute MLS-like limb radiances for a cloudy atmosphere [Wu et al., 2006]. The 1-D here implies that atmospheric and cloud variables vary only vertically. The model assumes spherical ice particles in cloud layers and derives cloud volume absorption/scattering coefficients and phase functions from the Mie solution. Multiple scattering effects are accounted for through an iterative approach of solving the RT equation [Wilheit et al., 1982; Yeh et al., 1990] but polarization effects are neglected. Cloud particle size distributions (PSDs) are based on the parameterization developed by McFarquhar and Heymsfield [1997, hereinafter MH97]. The 1-D radiance model takes into account the two sidebands (232.5 and 246.9 GHz) with a 50% sideband ratio, but FOV effects are neglected.

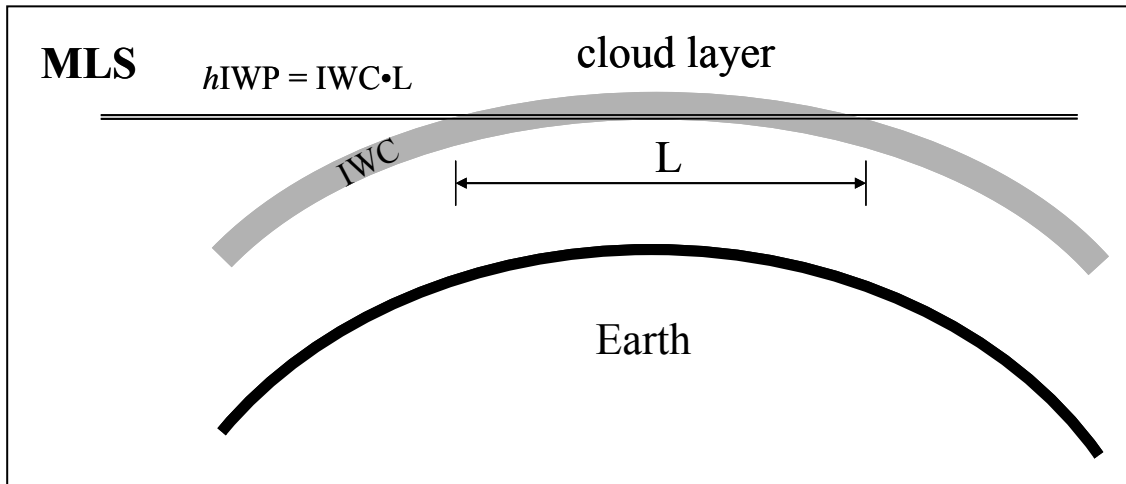


Figure 1. Schematic diagram to illustrate the radiative transfer of MLS radiance through an atmosphere with a single cloud layer. T_{cir} is proportional to horizontal ice water path ($hIWP$). Knowing the characteristic cloud length, L , we may relate T_{cir} directly to IWC of the cloud layer near the tangent height (see text).

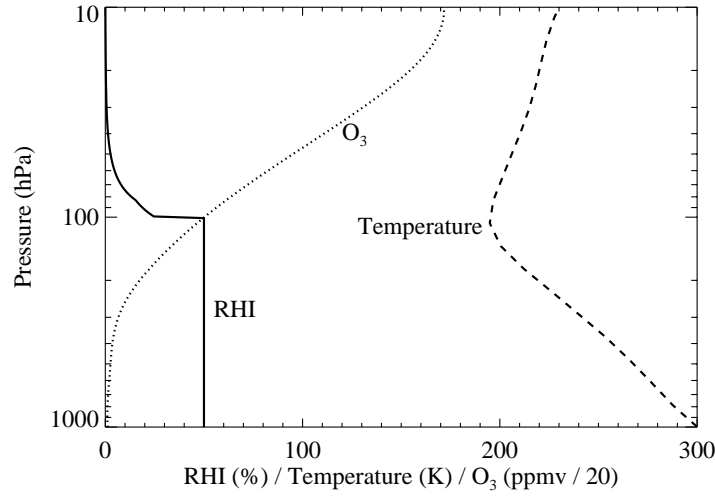


Figure 2. The model temperature, RH and O_3 profiles used for the cloudy-sky radiance calculations. The O_3 profile is in ppmv but multiplied by 20 on this scale.

The model atmosphere contains a single 2-km thick cloud layer centered at altitude h_0 with a trapezoid vertical distribution that is uniform in the center 1 km and linearly decays in the top and bottom half km (Appendix B). In simulating T_{cir} variations with respect to IWC, we change cloud ice amount by multiplying this cloud profile with different IWC values. For this particular cloud profile, horizontal ice water path ($hIWP$) at $h_t=h_0$ is proportional to the mean IWC in the cloud layer and the equivalent length of the cloud layer L is ~ 200 km. The background clear-sky atmosphere is based on the tropical temperature profile from the CIRA (COSPAR International Reference Atmosphere) reference atmosphere for January [Fleming et al., 1988]. In addition, the model assumes 100% in-cloud RH but 50% elsewhere at pressures > 100 hPa. Above that pressure level, RH is relaxed to a nominal stratospheric profile. The model also includes O_3 because of its non-negligible contributions in the 240 GHz channel, which along with the model T and RH profiles are given in Figure 2.

Figure 3 shows the T_{cir} profiles calculated for the double-sideband 240 GHz window channel (232.5 and 246.9 GHz) in a cloudy-sky atmosphere where the 2-km cloud layer is

centered at 16 km altitude. As shown in Figure 3a, the cloud perturbs limb radiances by increasing (decreasing) brightness temperature at tangent heights above (below) ~ 9 km where the background radiances are relatively low (high). The amplitude of T_{cir} increases with cloud ice amount at small values but reaches saturation at $hIWP \sim 15 \text{ kg/m}^2$ or $IWC \sim 100 \text{ mg/m}^3$ as the cloud becomes opaque.

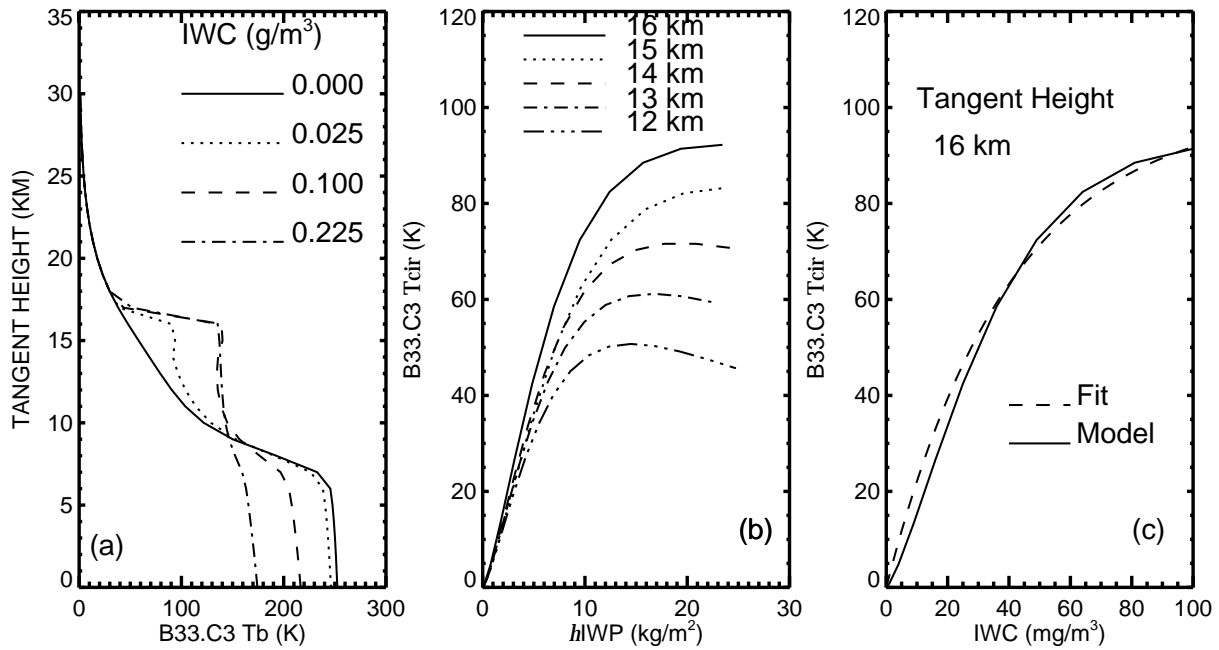


Figure 3 (a) Modeled limb radiances of MLS B33.C3 (232.5 and 246.9 GHz), the window channel of the 240 GHz radiometer. A 2-km cloud layer is placed at 16 km with a trapezoid distribution (see Appendix B). (b) T_{cir} - $hIWP$ relations for different tangent heights (c) Modeled (solid line) and fitted (dashed line) B33.C3 T_{cir} -IWC relation at $h_t = 16$ km.

In essence, MLS T_{cir} is a measure of $hIWP$, a column of cloud ice along the line-of-sight (LOS). Figure 3b shows that T_{cir} is linearly proportional to $hIWP$ at small values with a nearly constant slope for all the tangent heights. One can convert T_{cir} to the mean cloud IWC using the characteristic length L of the cloud layer. In this $h_0=16$ km case, we have $L \approx 200$ km at $h_t=h_0$

(Appendix B) and $Tcir(h_t) \propto IWC(h_0=h_t)$, which is the basis for the modeled $Tcir$ -IWC relation at $h_t=16$ km in Figure 3c. To obtain the $Tcir$ -IWC relation at a different tangent height, we place the cloud layer at that tangent height and repeat the same calculations as for the $h_t=16$ km case. In V2.2 IWC retrieval we approximate the modeled $Tcir$ -IWC relation with

$$Tcir = Tcir_0 (1 - e^{-IWC/IWC_0}) \quad (1)$$

where the fitting parameters $Tcir_0$ and IWC_0 are given in Table 1.

The $Tcir$ -IWC relations are similar to those of the 2-km layer case if IWC has an extensive vertical distribution and decreases exponentially with height, or $IWC \propto e^{-z/H_0}$, where H_0 is the mean scale height of IWC profiles. Such an IWC vertical distribution is consistent with the climatology from in-situ observations in the upper-troposphere [Heymsfield and Donner, 1990; McFarquhar and Heymsfield, 1996], and H_0 is ~ 2 km in the tropical upper troposphere but becomes steeper (~ 1 km) near the tropopause. Assuming $IWC \propto e^{-z/H_0}$, we find that $Tcir$ is still proportional to the IWC at pointing tangent height except with a characteristic length of $L \approx 200\sqrt{H_0}$ (Appendix B). Thus, for most cloud ice distributions in the upper troposphere, Eq. 1 is a good approximation to the MLS $Tcir$ -IWC relations with the characteristic horizontal length L varying between 200 and 300 km for the averaged IWC.

Two-Dimensional (2-D) Model

To better understand cloud inhomogeneity effects on MLS IWC retrieval and spatial resolution, we also developed a 2-D cloudy-sky RT model, based on the 2-D clear-sky model [Read et al., 2006]. We modified the 2-D clear-sky model to include contributions from cloud emission and scattering volume coefficients, as expressed in Eq. (3) of Wu et al. [2006]. The same assumptions and approximations are applied to cloud scattering calculations as in the 1-D

model, but with only single scattering. This 2-D cloudy-sky model is employed to simulate the V2.2 *Tcir*.

IWC-induced *Tcir* is linearized about the mean state $Tcir_0$ through the Taylor expansion to yield a linearized 2-D model, mathematically, written as

$$5 \quad Tcir(P_{tan}, IWC) = Tcir_0(P_{tan}, IWC_0) + \sum_{i,k} WF(x_i, z_k, P_{tan}, IWC_0)(IWC - IWC_0) \quad (2)$$

where indices i and k denote model discrete horizontal and vertical coordinates, namely in x and z . $WF(x_i, z_k, P_{tan}, IWC_0)$ is the first derivative of *Tcir* with respect to IWC, also called the IWC weighting function (WF), which is linearized at IWC_0 and given by

$$\begin{aligned} WF(x_i, z_k, P_{tan}, IWC_0) &= \left. \frac{\partial T_{ik} cir}{\partial IWC} \right|_{IWC=IWC_0} \\ &= \left(\frac{\partial T_{ik} cir}{\partial \beta_{ca}} \bullet \frac{\partial \beta_{ca}}{\partial IWC} + \frac{\partial T_{ik} cir}{\partial \beta_{cs}} \bullet \frac{\partial \beta_{cs}}{\partial IWC} \right) \bigg|_{IWC=IWC_0} \end{aligned} \quad (3)$$

10 where $T_{ik} cir$ is the component of *Tcir* at location (x_i, z_k) and $Tcir = \sum_{i,k} T_{ik} cir$. The $T_{ik} cir$ derivatives with respect to cloud volume absorption (β_{ca}) and scattering (β_{cs}) coefficients, $\partial T_{ik} cir / \partial \beta_{ca}$ and $\partial T_{ik} cir / \partial \beta_{cs}$, are computed analytically using the formula developed for clear-sky volume absorption coefficients [Read et al., 2006]. The derivatives $\partial \beta_{ca} / \partial IWC$ and $\partial \beta_{cs} / \partial IWC$ are derived from the Mie solution and the MH97 PSD [Wu and Jiang, 2004]. In
15 addition to its ability of handling cloud inhomogeneity, the 2-D RT model contains the most updated instrument parameters (e.g., FOV, sideband ratios). Therefore, we here use the modeled 2-D WFs to assess instrument spatial resolution, 1-D model error, and cloud inhomogeneity effects on the V2.2 IWC retrieval.

The 2-D RT model, especially with cloud scattering calculations, is computationally intensive in time and memory. Due to limited computing resources, we choose the resolution of IWC profiles to be 0.5° (~ 50 km) along track and 24 pressure levels per decade (~ 0.67 km) and use the same background atmospheric profiles as in the 1-D model [Figure 2] for all 2-D calculations.

2.3 Spatial Resolution

To quantify spatial resolution of the V2.2 IWC measurements, we restrict our study to optically-thin situations at 215-83 hPa where cloud ice does not saturate limb radiances. In these cases the WFs of the linearized 2-D model (Eq. 3) characterize how T_{cir} is contributed horizontally and vertically. As shown in Figure 4, the WFs for T_{cir} at 215-83 hPa are broadened horizontally over a long limb path (200-400 km along track) and vertically by the instrument FOV (~ 3.2 km at 240 GHz). At $P_{tan}=215-83$ hPa, the WFs are mostly positive with maximum near the tangent point. In this calculation, we assume a 10 mg/m^3 IWC uniformly distributed at pressures >83 hPa and force the IWC profile to drop sharply (with a scale height of 0.5 km) above 83 hPa since clouds rarely reach altitudes above 18 km. The 10 mg/m^3 value is arbitrarily chosen to represent an optically-thin cloud field. As long as the T_{cir} -IWC relation remains in the linear regime ($\text{IWC} < \sim 50 \text{ mg/m}^3$), the morphology of the WFs at 215-83 hPa does not vary much.

Although the WFs at 215-83 hPa extend widely and deeply into very high altitudes, only those near the tangent height are important because of the $\text{IWC} \propto e^{-z/H_0}$ distribution. Thus, we can approximate these WFs with rectangular boxes as shown in Figure 4. As long as the $\text{IWC} \propto e^{-z/H_0}$ distribution holds in the upper troposphere, T_{cir} will be contributed mostly from IWC in the volume near the pointing tangent height. The horizontal and vertical resolutions of

these rectangular boxes are approximately given by $200\sqrt{H_0}$ and $3.2+1.8/H_0$, respectively (Appendix B). According to in-situ observations, IWC profiles tend to have $H_0 = \sim 1$ km above ~ 14 km and $H_0 = \sim 2$ km below that height.

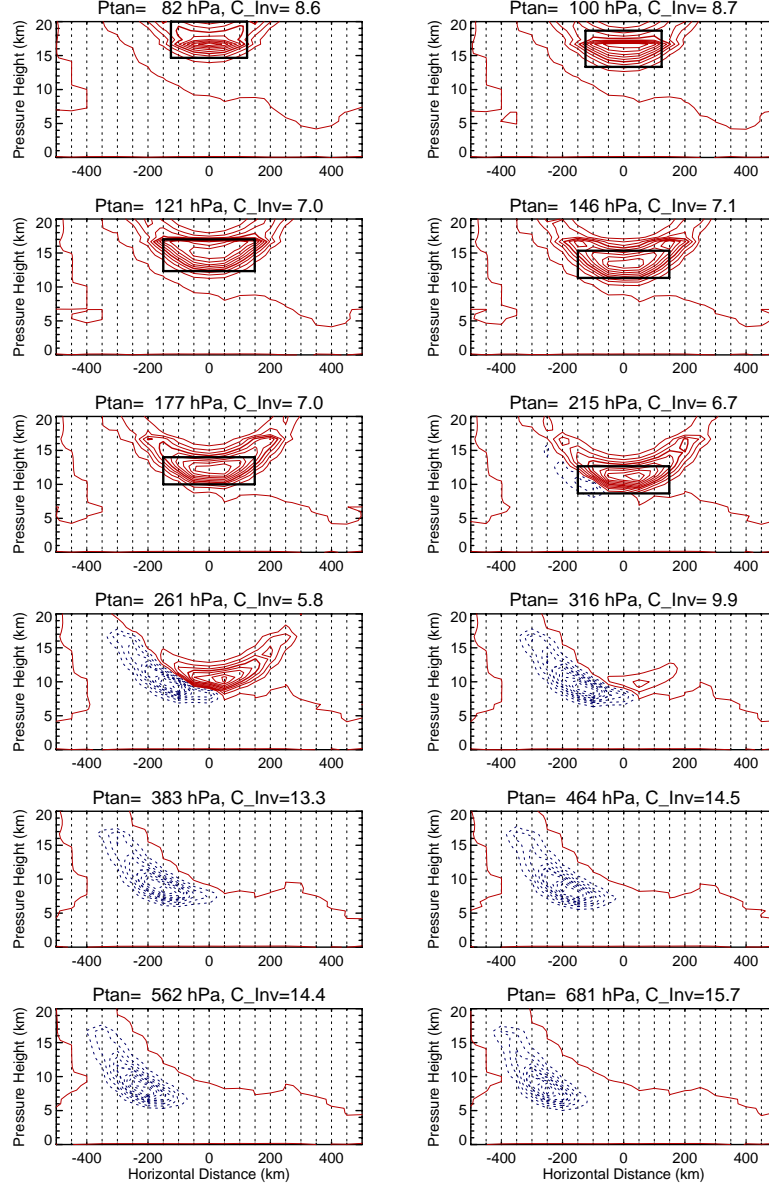


Figure 4 IWC weighting functions (in $\text{K}\cdot\text{g}^{-1}\text{m}^3$), or $WF(x_i, z_k, P_{\text{tan}}, IWC_0)$, for the 2-D RT model [Eq.2] linearized at $IWC_0=10 \text{ mg/m}^3$. The 2-D model has 21 IWC profiles (indicated by the dotted lines) and 35 vertical levels (24 levels per decade pressure in hPa). Red (Blue) contours show the positive (negative) weights with the contour interval (in $\text{K}\cdot\text{g}^{-1}\text{m}^3$) indicated in the title of each panel. In this example, MLS views from the negative-distance side and is only sensitive to clouds on the MLS side of tangent point at low h_t where the radiance cannot penetrate through the limb. For this calculation a uniform distribution ($IWC_0 = 10 \text{ mg/m}^3$) is assumed up to ~ 83 hPa but drops to zero sharply above that pressure level. Contributions at pressures < 74 hPa (~ 18 km) are zeroed in these plots because clouds rarely exceed that altitude.

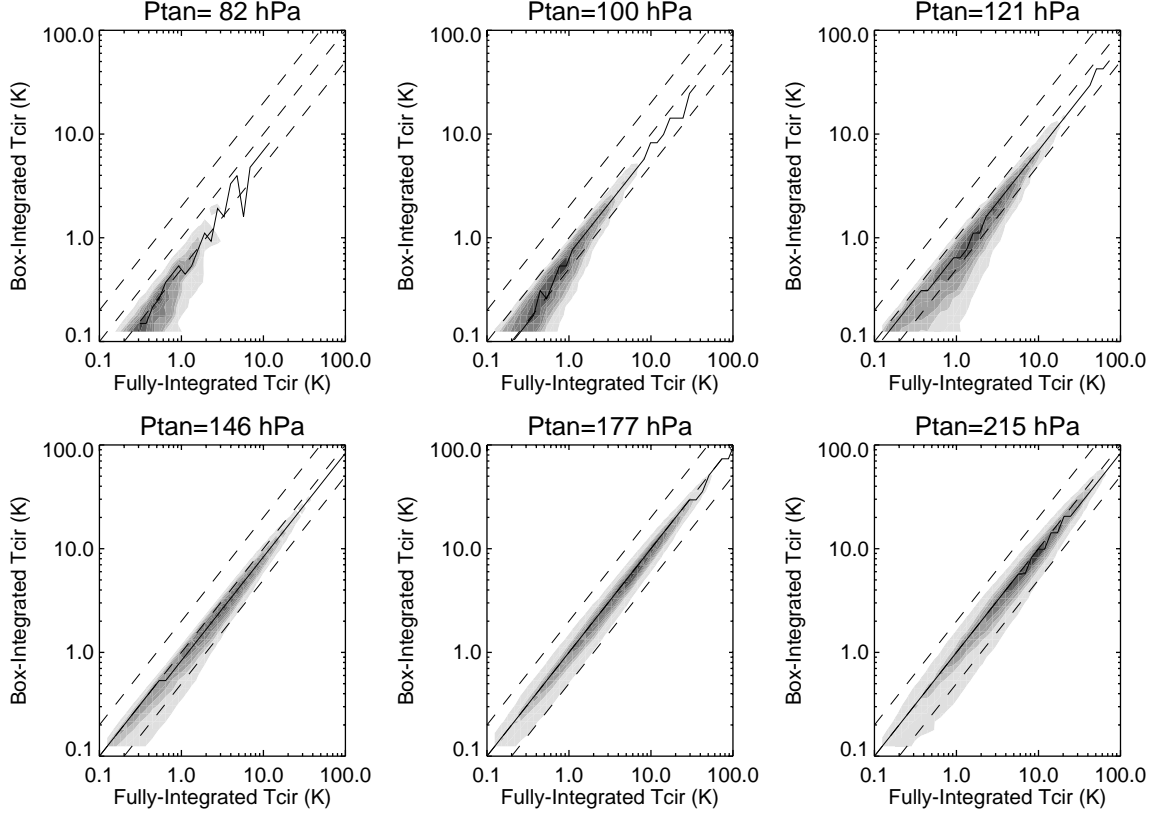


Figure 5. Comparisons of T_{cir} computed from the full 2-D WF and from the 2-D box averaging for six tangent pressures between 83 and 215 hPa. The number density distribution is shaded with the maxima connected by the solid line. The dashed lines indicate ratios of 2:1, 1:1 and 1:2.

5 To evaluate the rectangular-box approximation under realistic cloud fields, we use 50km-averaged CloudSat IWC profiles as the input to the WFs in Figure 4, and compare the fully-integrated T_{cir} (from convolving the 2-D WFs with CloudSat IWC profiles) with boxcar-averaged T_{cir} . We further adjust the horizontal and vertical dimensions of the rectangular box to best fit the fully-integrated T_{cir} [Figure 5]. The final horizontal and vertical dimensions of the

10 rectangular boxes are plotted in Figure 4 as the V2.2 IWC measurement volume at each pressure level. They are very close to the values estimated from $IWC \propto e^{-z/H_0}$ distributions, yielding the (horizontal, vertical) resolutions of (300, 4), (250, 4), and (200, 5) km at 215-147, 121, 100-83 hPa, respectively.

The box-averaged and the WF-convolved T_{cir} 's agree quite well [Figure 5], showing overall good 1:1 correlation for a large dynamic range. At 215-147 hPa, there are relatively small (<20%) biases introduced due to the boxcar approximation. The bias increases to ~50% at 121 hPa, 50-100% at 100 hPa and ~100% at 83 hPa, showing systematically smaller values in the box-averaged T_{cir} , which mean that the V2.2 IWC is likely biased high as the box mean.

Figure 4 also reveals limitations of the simple IWC retrieval technique used in the V2.2 algorithm. The V2.2 IWC retrieval assumes that T_{cir} increase monotonically with IWC, which is only valid at tangent pressures < 261 hPa where the 2-D WFs are dominated by positive contributions. At 261 hPa and below, negative weights contribute a significant portion of T_{cir} , which offset the positive contributions, causing reduction in T_{cir} sensitivity to IWC. Depending on the amount of cloud ice in the path, generally speaking, the 240-GHz radiance has a poor sensitivity to cloud ice at these transition tangent pressures (383-261 hPa) [Wu and Jiang, 2004]. At tangent pressures >383 hPa, the WFs are dominated by negative contributions because clouds tend to scatter upwelling radiation out of the MLS LOS, resulting in a reduction in the upwelling radiance contributed by clear sky. Hence, the T_{cir} 's at these tangent heights are negative and can be used to retrieve a partial column of cloud ice (above ~6 km). This cloud ice retrieval is beyond the scope of the paper and will be discussed in a future study.

2.4 V2.2 IWC Retrieval

In the V2.2 algorithm we retrieve IWC at pressures ≤ 215 hPa from the 240-GHz T_{cir} at high tangent heights. Converted directly from the T_{cir} , the V2.2 IWC represents a volume-averaged quantity of which the spatial dimensions are characterized by the rectangular boxes in Figure 4. The retrieval are based on the T_{cir} -IWC relations fit to Eq. 1 and the parameters (T_{cir_0} , IWC_0) are given in Table 1.

Table 1. Model coefficients for the V2.2 *Tcir*-IWC relations

<i>Ptan</i> (hPa)	<i>Tcir</i> bias (K) ^a	<i>Tcir</i> ₀ (K)	IWC ₀ (mg/m ³)
83	-1.5	100	40
100	-2.2	100	40
121	-2.5	100	43
147	-3.2	90	55
177	-4.2	80	69
215	-6.0	70	70
261	-7.5	50	50

a) The *Tcir* bias is estimated from the real data, and interpolated values will be used if MIF tangent pressures are not at these pressures. Cause(s) of the *Tcir* bias will be discussed later in systematic uncertainty section.

As discussed later in section 3.1, the 240-GHz *Tcir* contains a bias that varies pressure and latitude. Prior to the V2.2 IWC retrieval, an estimated *Tcir* bias is removed but with fixed values for all latitudes [Table 1]. The corrected *Tcir* are then averaged onto the standard horizontal (1.5° along track) and vertical (12 level per decade) grids, and converted to IWC using the modeled *Tcir*-IWC relations (Eq. 1). Since each MLS scan is closely associated with a retrieval grid box, the binning does not degrade the horizontal resolution of MLS IWC. MLS scans provide very dense (every ~300 m) vertical sampling in the upper troposphere and lower stratosphere (UT/LS), and binning *Tcir* into the standard 12-levels-per-decade grid does not degrade IWC vertical resolution.

2.5 MLS IWC Data Usage

The V2.2 IWC are reported in the HDF-EOS (version 5) Level 2 Geophysical Product (L2GP) IWC file under the swath name of IWC with units of g/m³. The standard IWC product has a useful vertical range between 261 and 68 hPa. Along with the data field in the L2GP file, the IWC precisions are pre-estimated values from one test day and are identical in all IWC files. These precisions are only rough estimates, and the user should screen the data and compute a more accurate precision on a daily basis (discussed in the next two paragraphs). The other quality fields, “Status”, “Quality”, and “Convergence”, are not used in the V2.2 IWC L2GP file. To

exclude IWC measurements affected by bad pointing retrievals, the user is recommended to check the “Status” of temperature data for data quality control and only use the profiles with the temperature “Status” equal to an even number [Schwartz et al., 2007]. The L2GP file also reports an IWP product as a separate swath, named “IWP”, which is retrieved from the 240 GHz T_{cir} at low tangent heights for a partial column of cloud ice above ~6 km; validation of the IWP product will be carried out in a separate paper.

The MLS IWC data in the L2GP file contains negative values as expected for noisy measurements. No cloud mask or screening is applied to the data in the L2GP file. These negative values need to be retained to properly produce average values, as well as to estimate the IWC precision and bias as described in the following.

To screen the MLS IWC data, the user needs to compute latitude-dependent IWC precision (σ) and bias (μ) from daily measurements, for which we recommend a 2σ - 3σ method that has been successfully used by the MLS team. First, compute and remove latitudinal-varying IWC biases at each pressure level. Since clouds detectable by MLS are generally less than 20% of the total measurements at most latitudes, one can determine the σ and μ of IWC for every 10° latitude bin by iteratively rejecting the outliers greater than 2σ . The iteration may start with $\mu=0$ and use all measurements in the latitude bin to compute the first σ . In the next iteration, reject the measurements greater than 2σ above μ , and re-evaluate σ and μ from the remaining measurements. Repeat these steps to refine the σ and μ until the solutions to σ and μ are converged. The convergence is usually reached within 5-10 iterations. The final σ and μ give the estimated IWC precision and bias for this bin. Second, interpolate the σ and μ obtained for 10° latitude bins to the measurement latitudes, and remove the bias for each individual measurement.

In the final step, apply the 3σ threshold for cloud detection. In other words, only values with $IWC > \mu + 3\sigma$ are classified as reliable cloud ice measurements. The 3σ threshold is needed for reliable cloud detection since a small percentage (1%) of clear-sky noise can yield a large percentage error for cloud statistics.

5 **2.6 V1.5 and V2.2 Differences**

There are two major differences between V1.5 and V2.2 IWC retrievals. The first is that the RT model used by V2.2 is greatly improved to produce a better precision for T_{cir} and IWC. The second difference is that the V2.2 T_{cir} -IWC relation accounts for nonlinearity whereas the V1.5 relation is linear. As a result, the V1.5 retrieval systematically underestimates IWC at large
10 values. For this validation study, we also developed an intermediate IWC retrieval (called V1.5c) based on V1.5 data, which has the similar noise characteristics to V1.5 but has the nonlinearity correction as in V2.2.

Figure 6 shows a comparison of V1.5, V1.5c, and V2.2 IWC for 28 January 2005 at 147 hPa where the bias has been removed using the 2σ - 3σ screening method. On this particular day the
15 V1.5 and V1.5c 3σ envelopes show a significant variation with latitude with generally larger (or worse) values than those in V2.2 IWC at most latitudes, indicating the improved IWC precision and better cloud detectability with the V2.2 retrieval. In addition, the V2.2 3σ envelope is more uniform across latitude, whereas the V1.5 precision is noticeably worse at wintertime mid and high latitudes. As expected, the V1.5c data have similar precision to that in V1.5, but more
20 measurements with $IWC > 20 \text{ mg/m}^3$.

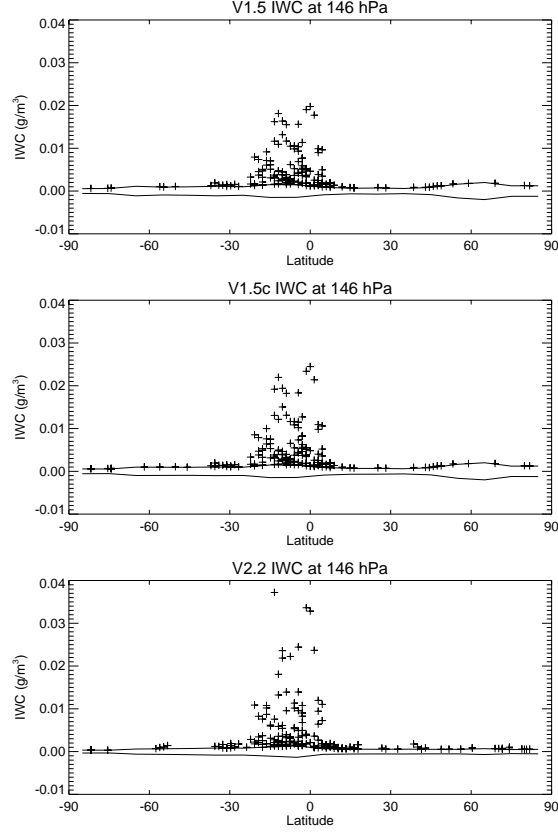


Figure 6 Latitudinal distribution of MLS v1.5, v1.5c, and V2.2 IWC at 147 hPa on 28 January 2005. A latitudinally-dependent bias has been removed in these plots. The solid curves are the 3σ envelopes for clear-sky noise and IWC measurements above the 3σ threshold are significant cloud hits.

5 Figure 7 compares the normalized probability density functions (PDFs) of V1.5, V1.5c and V2.2 IWC for five latitude bins and six pressure levels. Measurement noise and cloud statistics are reflected in these PDFs. The sharply rising PDF at small IWC values is due to measurement noise. To examine MLS IWC noise more closely, we fold the PDF of negative IWC to the positive side, and the rising PDF for small values is consistent with the noise statistics of the

10 negative IWC values. Figure 7 shows that V2.2 IWC has better precision than V1.5 IWC at high latitudes and at pressures <147 hPa. The improved precision allows MLS to detect some clouds not seen with V1.5, especially at mid and high latitudes (82°S - 45°S and 82°N - 45°N). At large IWCs, V1.5c exhibits a cloud PDF tail similar to V2.2 as expected from the correction made for the T_{cir} -IWC nonlinearity.

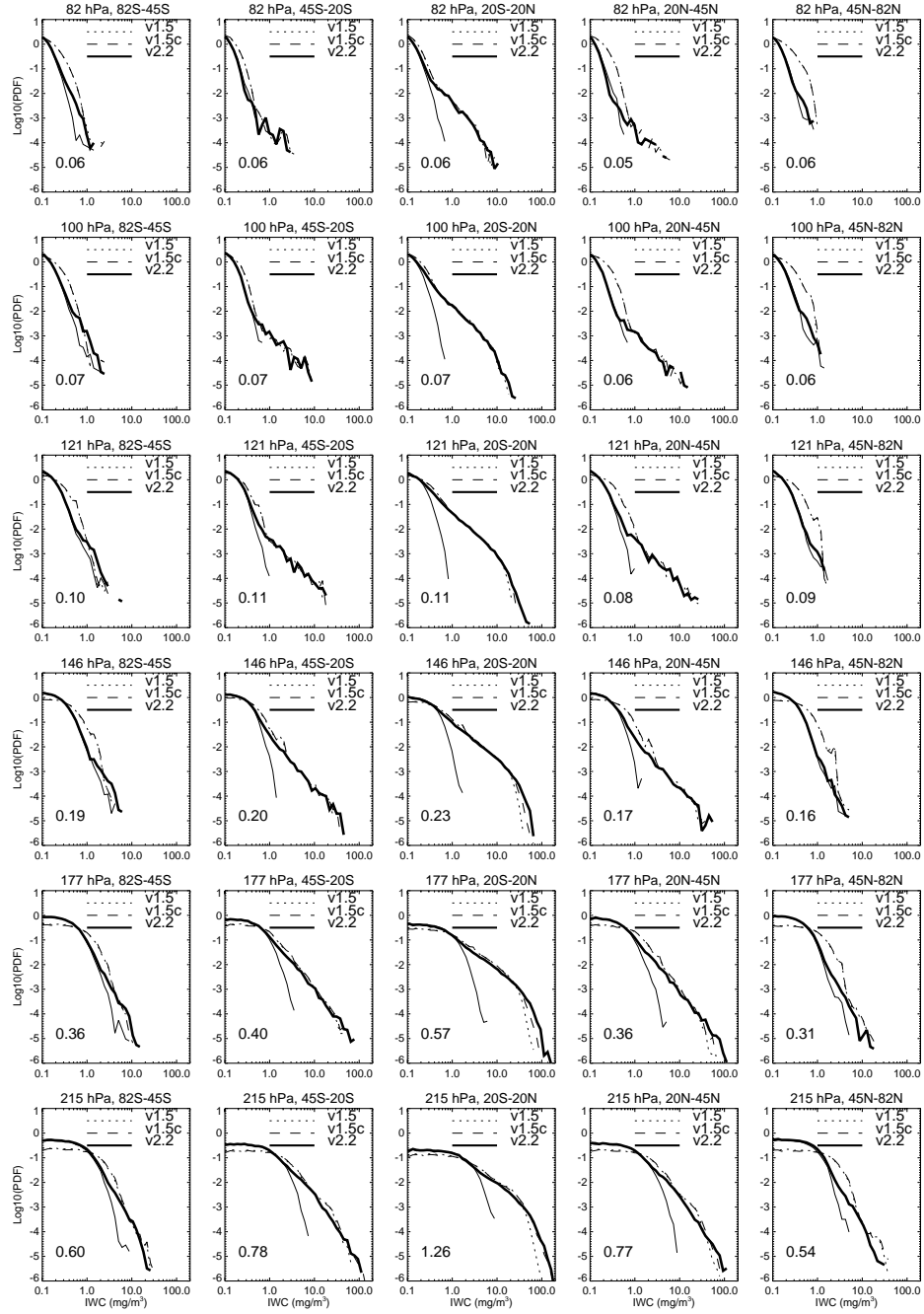


Figure 7. PDFs of MLS V1.5 (dotted), V1.5c (dashed), V2.2 (thick solid) IWCs for five latitude bins and six pressure levels. A total of 92 days of MLS IWC measurements are compiled for these statistics, which account for the days when both V1.5 and V2.2 data are available. Biases have been removed in these calculations as described in the text. The thin solid line in each panel corresponds to the PDF of negative V2.2 IWC values, but is folded to the positive side to compare with the V2.2 IWC noise. The V2.2 IWC PDF (thick solid line) becomes statistically insignificant where it falls on the thin line. The estimated standard deviation for the V2.2 IWC (in mg/m^3) is indicated in each panel.

3 Estimated Precision and Systematic Uncertainties

3.1 *Tcir* Bias and Precision

MLS 240 GHz *Tcir* is affected by errors in the radiance measurements [Jarnot et al., 2006] and the modeled radiance [Read et al., 2006], of which the latter often dominates the total error budget. We can estimate *Tcir* bias and precision (μ_{tcir} and σ_{tcir}) empirically from data using the 2σ - 3σ screening method described for IWC, and results from the V2.2 retrieval and the simulation are shown in Figure 8. The *Tcir* errors are characterized separately for the tropical (30°S-30°N) and extratropical (30°-82°) bins. At 15 km, both tropical and extratropical PDFs of V2.2 *Tcir* [Figure 8(a) and (c)] exhibit a Gaussian-like distribution at small positive and negative *Tcir* values. Because at this altitude clouds can only induce positive *Tcir*, the PDF of negative *Tcir* should have a Gaussian distribution as expected for simple white noise. In the tropical case [Figure 8(a)], the PDF of negative *Tcir* agrees well with the Gaussian distribution for the estimate noise. In the extratropical case [Figure 8(c)], the PDF of negative *Tcir* follows the Gaussian up to approximately -1.5 K before showing some deviation. The non-Gaussian PDF of negative *Tcir* implies greater probability of false cloud detection than suggested by the standard deviation. In both tropical and extratropical cases, *Tcir* precisions are much larger than the precision (0.15 K) of the calibrated radiance, indicating dominance of the modeled radiance error. Comparing V2.2 with the simulated data [Figure 8(b) and (d)], we find that the algorithm generally produces a better precision for the simulated data than for the real data, but in both cases the *Tcir* precision is worst at $h_t \sim 8$ km.

The V2.2 *Tcir* shows a large (-13 K) negative bias in the tropical bin, which is somewhat smaller (-6 K) in the extratropical bin [Figure 8(b)]. The V2.2 Level 2 algorithm corrected this *Tcir* bias prior to the IWC retrieval [Table 1], but with the same bias profile for all latitudes.

Hence, latitude-dependent T_{cir} biases are likely propagated to the retrieved IWC, which the user needs to remove on a daily basis using the screening method described in section 2.5.

We conducted a series of sensitivity tests to investigate the cause of the negative bias in the 240-GHz T_{cir} . Various families of uncertainty are tested to assess the T_{cir} error, including R2-
5 R3 FOV offset, R1-R3 FOV offset, sideband ratios, gain compression, standing waves from calibration sources, scan jitter, antenna transmission, FOV shape, and spectroscopy. More details about these systematic errors can be found in Appendix B of Read et al. [2007]. In these tests we evaluated the induced limb radiance errors by perturbing instrument and RT model parameters within their uncertainties. In addition, we carried out two more sensitivity studies that explore
10 impacts of the retrieved T and H_2O errors. Because the V2.2 algorithm caps the tropospheric RHi at 110% in the T_{cir} calculations, the T retrieval error can induce systematic T_{cir} errors through the RHi capping even though the H_2O mixing ratio retrieval is perfect. In fact, the H_2O retrieval may have a bias of 20-30% in the upper troposphere [Read et al., 2007]. The derived 240-GHz T_{cir} is particularly sensitive to T and H_2O errors at $h_t=6-12$ km where the window channel has
15 the maximum sensitivity to H_2O continuum emission. In one test, we perturb the T profile by -2 K as expected for the T retrieval bias [Schwartz et al., 2007]. In the other test, we reduce the RHi value by -30% in the troposphere corresponding to the worst retrieval cases [Read et al., 2007].

Most of the tests produce a negligible error in T_{cir} except for the sources shown in Figure 9. The R2-R3 offset and dry-air continuum errors can induce significant (-3 K and +2 K,
20 respectively) T_{cir} biases, which are still too small to explain the observed negative T_{cir} bias. Systematic errors from the retrieved T and H_2O are capable of generating the observed large negative T_{cir} error although the bias peaks at a slightly lower tangent height than observed. We find that the T_{cir} bias is very sensitive to the T retrieval error at 10-12 km. As shown in Figure 9,

the error in the 10-12 km layer contributes -7 K to the T_{cir} bias, compared to -13 K if the entire troposphere is perturbed. MLS T retrieval uncertainty remains as a major error source for the derived T_{cir} because the T error is semi-random with a vertical correlation length of 2-3 km in the upper troposphere [Schwartz et al., 2007]. As a result, the vertically-correlated T error (~ 1 K) can induce a ~ 3 K T_{cir} error at 215 hPa, which is consistent with the precision estimate from the real data [Figure 8].

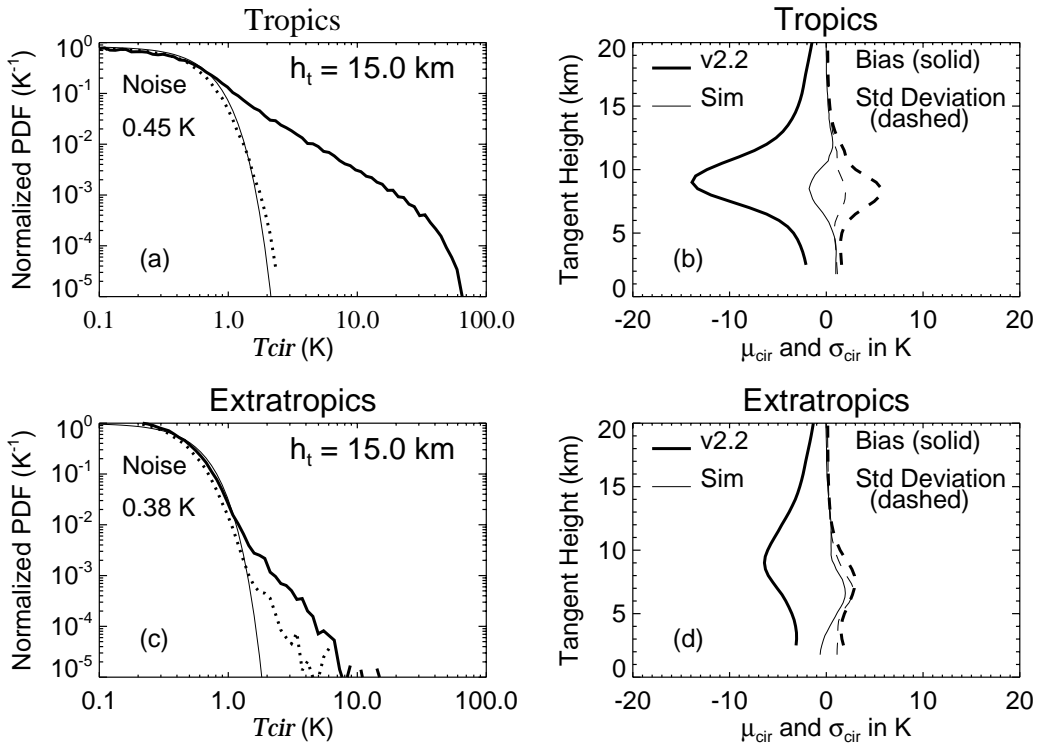


Figure 8 (a) PDF of V2.2 MLS 240-GHz T_{cir} at 15 km tangent height for the tropics (30°S - 30°N). The thick solid curve is the PDF of positive T_{cir} whereas the dotted curve is the PDF of negative T_{cir} but folded onto the positive side to compare with the T_{cir} noise fitted by a Gaussian function (thin line). The standard deviation of the Gaussian noise is indicated in the panel. A total of 92 days of data are analyzed and T_{cir} biases have been removed from the daily measurements. (b) Profiles of V2.2 240-GHz T_{cir} bias μ_{cir} (solid lines) and standard deviation σ_{cir} (dashed lines) estimated from the real data (thick) and simulation (thin) as a function of tangent height. (c)-(d) are same as in (a)-(b) except for the extratropics (82°S - 30°S and 30°N - 82°N).

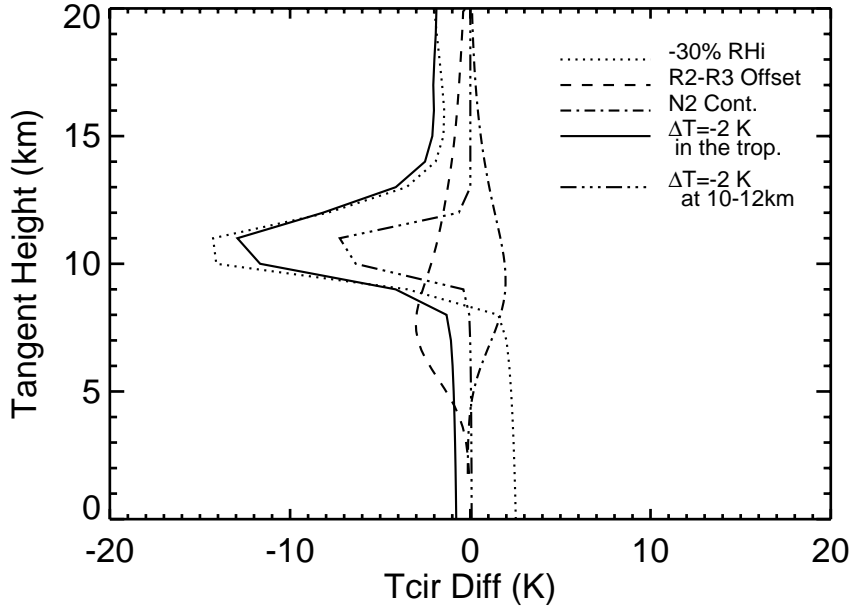


Figure 9. Systematic uncertainties estimated for MLS 240-GHz T_{cir} due to errors in T , RH_i , R2-R3 pointing offset, and dry continuum.

3.2 IWC Precision

All T_{cir} errors will be propagated directly into IWC through the T_{cir} -to-IWC conversion. A small T_{cir} error can cause a large IWC uncertainty in the IWC range where T_{cir} becomes saturated. Figure 10 plots the percentage error of T_{cir} and IWC as a function of IWC. The range where the V2.2 IWC is quantitatively useful is defined as IWC percentage error $< 100\%$. At small values, each IWC measurement must overcome the 3σ noise to be statistically significant.

This IWC range is referred to a single measurement, and an averaged IWC may produce useful values below this range. At large IWC values, the T_{cir} saturation causes great uncertainty in the retrieved IWC. At 261 hPa the IWC measurements are mostly qualitatively useful because the IWC percentage error exceeds 100% at $IWC > 30 \text{ mg/m}^3$ and the minimum detectable IWC is $\sim 12 \text{ mg/m}^3$ for the 3σ cloud detection. Hence, our validation studies will focus mainly on pressure levels at 215-83 hPa.

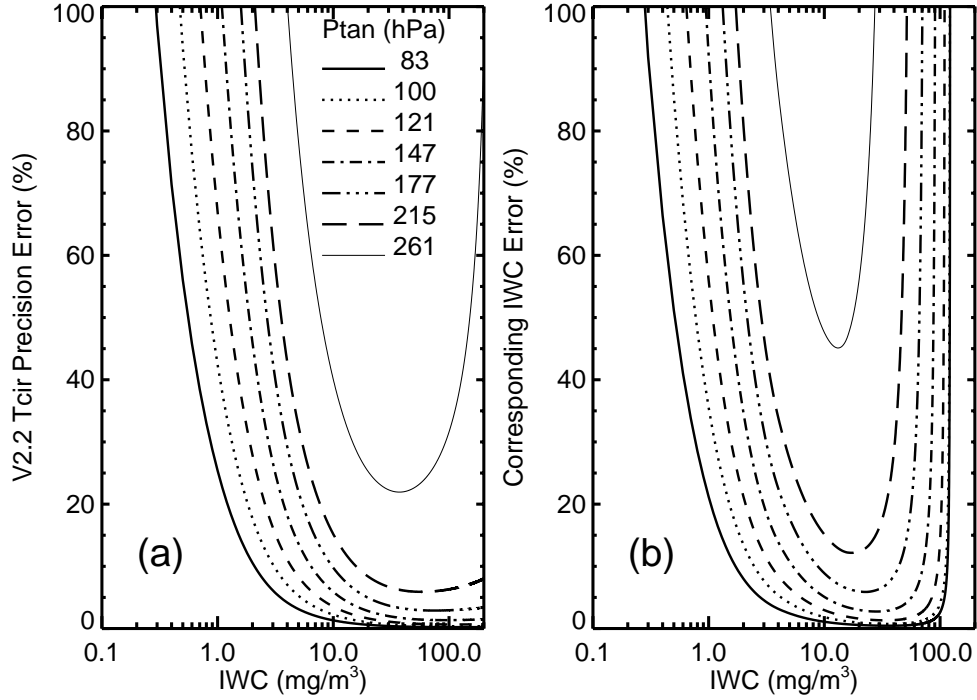


Figure 10. (a) Estimated V2.2 *Tcir* precision as a function of IWC in percentage for different tangent pressures. (b) Estimated V2.2 IWC precision as a function of IWC in percentage.

5

Table 2 Estimated MLS IWC precision and useful range

Pressure (hPa)	Precision (mg/m ³)				IWC range ^c (mg/m ³)
	V1.5 ^a	V1.5c ^a	V2.2 ^a	Simulation ^b	
83	0.08-0.14	0.08-0.15	0.06	0.09	0.02 -120
100	0.1-0.15	0.1-0.16	0.07	0.1	0.02 -120
121	0.14-0.2	0.14-0.2	0.1	0.1-0.2	0.04-110
147	0.3-0.4	0.3-0.4	0.2	0.3-0.5	0.1 - 90
177	0.6-0.9	0.7-0.9	0.3-0.6	0.6-1	0.3 - 70
215	1.2-1.8	1.3-1.9	0.6-1.3	1-1.6	0.6 - 50

a) These are typical 1σ precisions estimated for MLS data, where the better precision values are for the extratropics and the poorer values for the tropics. The precision for a particular measurement must be evaluated on a daily basis using the method described in the text.

b) These are the estimates of IWC precision from the simulation test. The range reflects differences between the tropical and extratropical retrievals.

c) A V2.2 IWC measurement is considered to be quantitatively useful if it is statistically significant and its precision is less than 100%. The useful range for a single V2.2 IWC measurement is limited by the uncertainty (2σ) about IWC biases from the screening method and by the *Tcir* saturation at the high end.

10

Table 2 summarizes typical single-measurement precisions and useful ranges of the V2.2 IWC for different pressure levels. The user needs to obtain a more accurate precision estimate from daily IWC measurements using the aforementioned screening method. The V2.2 IWC precision increases with pressure, which is consistent with the value expected from the *Tcir* error in Figure 8. MLS V1.5 and V1.5c exhibit similar precision in Table 2, both of which are worse than the V2.2 precision.

3.3 IWC Systematic Uncertainties

In this section we will focus on IWC systematic uncertainties for values $< 50 \text{ mg/m}^3$ from various sources of model and measurement errors.

Effects of Cloud Inhomogeneity

The modeled *Tcir*-IWC relations used in V2.2 are based on the 1-D model simulations for a layered cloud where MLS FOV and cloud inhomogeneity are ignored. To assess IWC uncertainties induced by cloud inhomogeneity, we must have realistic distributions of the IWC inhomogeneity. This requires large statistics of IWC variability over hundreds of kilometers in distance with vertical resolution better than 1 km, which are not available with airborne and ground-based observations. Because of MLS FOV and limb-view averaging, cloud spatial variability is more important than temporal variability. Thus, we use CloudSat IWC observations to assess effects of cloud inhomogeneity on MLS V2.2 IWC retrieval.

Using the CloudSat IWC profiles, we simulated MLS 240-GHz *Tcir* with the MLS 2-D RT model and compare the resulting *Tcir*-IWC relations with those used by V2.2. We randomly selected 2000 cases from CloudSat data in January 2007, binned the CloudSat IWC profiles to match MLS 2-D model grid sizes (0.5° horizontally and ~ 0.67 km vertically), and computed

MLS limb radiances and T_{cir} for each IWC averaged over the volume boxes in Figure 4. The resulting T_{cir} -IWC relations are shown and compared to the V2.2 relations in Figure 11.

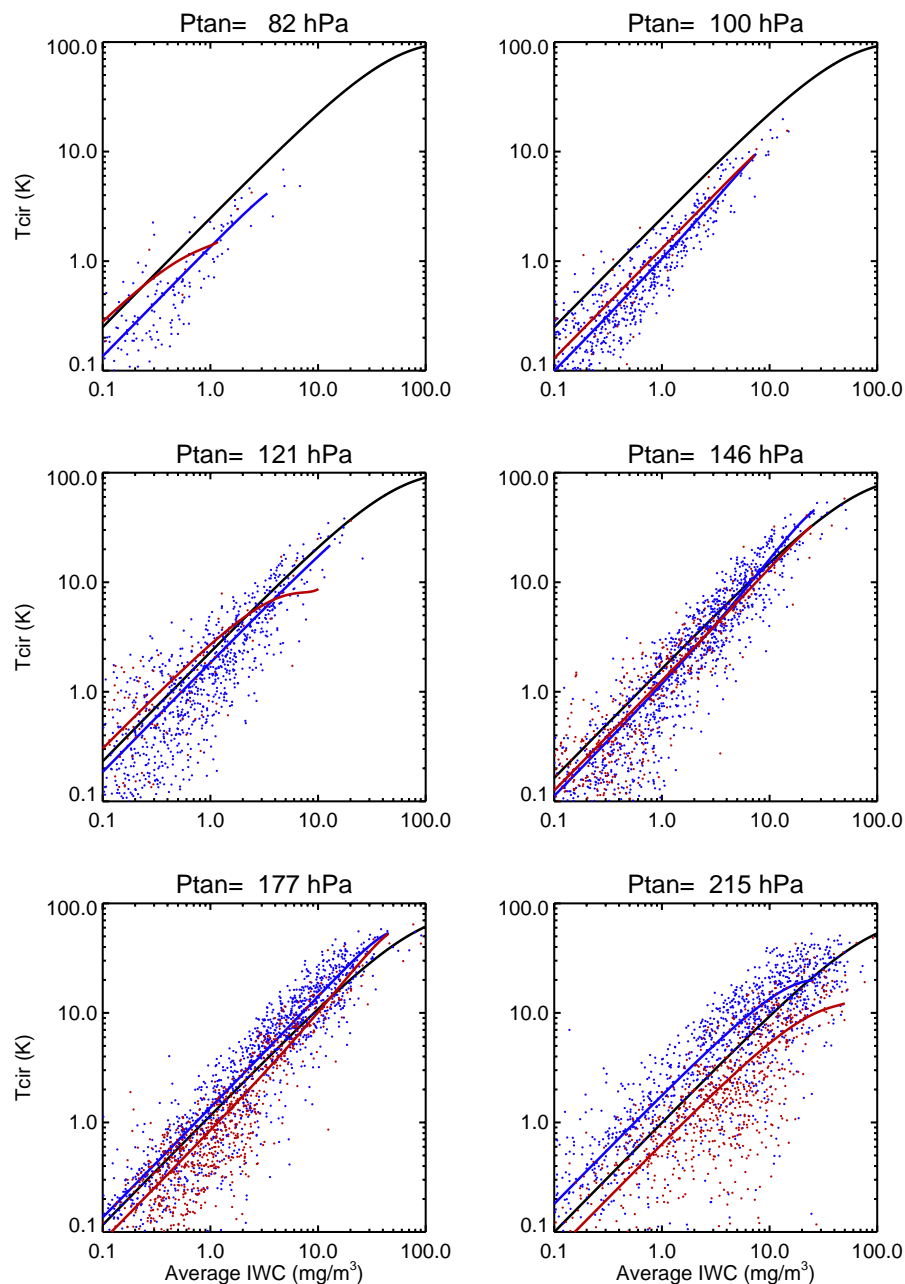


Figure 11. Comparison of the V2.2 T_{cir} -IWC relations (black curves) with those modeled by the 2-D RT model using CloudSat IWC profiles (dots). A total of 2000 randomly-selected CloudSat cases are used for the simulation: 1229 (red) from the tropics (20°S-20°N) and 771 (blue) from the extratropics. The IWC is averaged over the rectangular boxes as depicted in Figure 4. The colored curves correspond to the polynomial fit to the simulated T_{cir} -IWC relations in each latitude bin, and only data with $IWC > 0.1 \text{ mg/m}^3$ are used in the fitting.

As shown in Figure 11, the selected CloudSat cases cover a broad range of IWC values. The *Tcir*-IWC scatter reflects the uncertainty of individual V2.2 IWC measurements due to cloud inhomogeneity. As discussed above, interpreting V2.2 IWC as an average in the volume near the tangent point may induce error by registering it to a slightly wrong location. However, the inhomogeneity-induced IWC uncertainty appears to be random and can be reduced by averaging (e.g., monthly maps). For example, on a grid box of $5^\circ \times 10^\circ$ latitude-longitude, Aura MLS typically has a total of ~ 80 samples in the tropics during a month, which could reduce inhomogeneity-induced uncertainty by 9 times in the averaged IWC. The inhomogeneity-induced percentage error tends to increase at smaller *Tcir* values or at higher pressures, but less scatter is found for the simulations at 147 and 177 hPa than at other pressure levels. The inhomogeneity error can be corrected properly with a 2-D tomographic IWC retrieval on MLS *Tcir*, the technique currently used in MLS clear-sky gas retrievals [Livesey et al., 2006]. Such a sophisticated IWC retrieval is currently being studied and will be implemented in the future.

Figure 11 also reveals an inhomogeneity-induced scaling error in the V2.2 *Tcir*-IWC relations (Eq.1), which cannot be reduced by averaging. The scaling error is pressure-dependent, generally less than 30% at 177-121 hPa but can be as large as -70% at 100-83 hPa for the retrieved IWC. It is also latitude-dependent, especially at 177 and 215 hPa, showing that the *Tcir*-IWC relations have a smaller slope in the extratropical bin. At 215 hPa, ignoring cloud inhomogeneity, the V2.2 retrieval would overestimate IWC by 80% in the tropics but underestimate it by 40% in the extratropics, and the underestimation becomes worse for large IWC values. At 147 and 177 hPa, the V2.2 retrieval tends to underestimate IWC for values $< 10 \text{ mg/m}^3$ but overestimate it for values $> 10 \text{ mg/m}^3$, and the overestimation appears to increase with IWC for large values.

Uncertainties due to Particle Size Distribution (PSD)

To assess PSD uncertainties, we perturb parameters of the MH97 PSD by 2σ of their uncertainty, calculate the resulting changes in T_{cir} and IWC, and report the root-square sum (RSS) of T_{cir} and IWC changes as a function of IWC. As shown in Figure 12 the resulting T_{cir} and IWC changes are generally less than 40% in the linear regime of the T_{cir} -IWC relations. The IWC uncertainty increases sharply as T_{cir} approaches saturation. It exceeds 100% when IWC is greater than 30, 65, 100, 120, 160, 190, and 200 mg/m^3 at 261, 215, 177, 147, 121, 100, and 83 hPa, respectively.

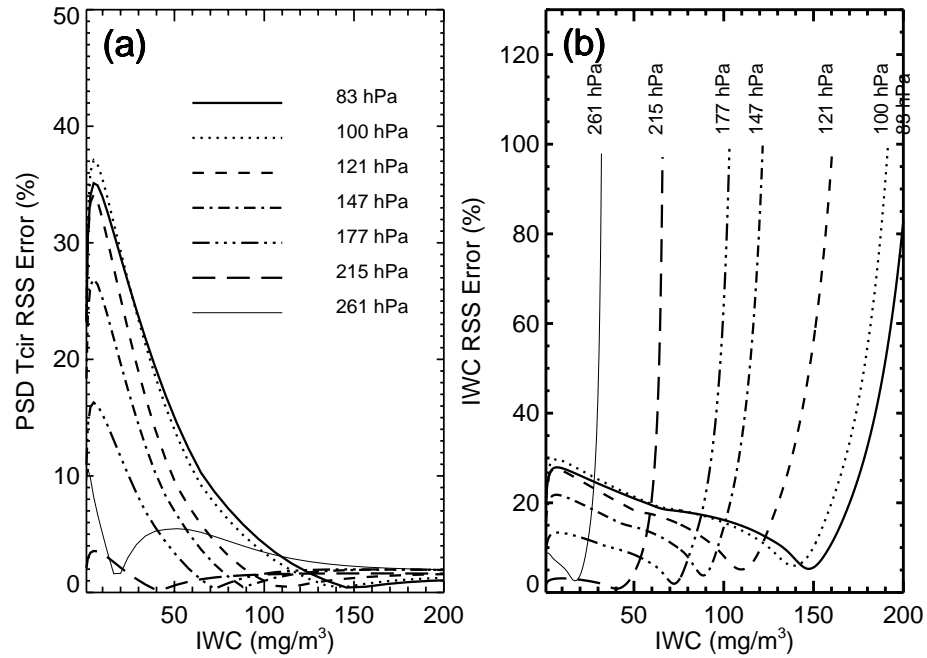


Figure 12. RSS of relative uncertainty (%) of the modeled T_{cir} -IWC relation due to error in MH97 PSD fitted parameters as a function of IWC: (a) T_{cir} and (b) IWC.

To evaluate uncertainty of the modeled T_{cir} -IWC relation due to different PSDs, we studied four parameterization schemes [MH97; Heymsfield et al., 2002; Donovan and van Lammeren, 2002; Field et al., 2005], which represent a variety of methods and clouds. The MH97 PSD parameterization, used in the MLS IWC retrieval, is based on in-situ measured size distributions

at 20°S–2°N latitudes, mostly from cirrus outflows. The size variable is the mass-equivalent diameter (D). As a function of T and IWC, the MH97 parameterization can produce a bimodal distribution and is valid for $-70^{\circ}\text{C} < T < -20^{\circ}\text{C}$. Bimodal PSDs, which further complicate microphysics of ice clouds [e.g., Platt, 1997], play a critical role in IWC remote sensing because cloud ice masses associated with the two modes are equally important and MLS 240 GHz measurement is mostly sensitive to T_{cir} induced by the large particle mode [Wu and Jiang, 2004]. Heymsfield et al. [2002, hereinafter H02] fit the in-situ data collected in the tropics and subtropics to a single Gamma distribution as a function of particle maximum dimension (D_m). The resulting PSDs also depend on T and IWC but are only valid for $T > -50^{\circ}\text{C}$ with the best results at $-40^{\circ}\text{C} < T < 0^{\circ}\text{C}$. H02 yields a better size distribution parameterization than MH97 for particle sizes > 2 mm. Donovan and van Lammeren [2002, hereinafter DL02] developed a bimodal PSD parameterization using lidar-radar remote sensing data at the Atmospheric Radiation Measurement Program’s Southern Great Plains (ARM-SGP) (36.4°N). The size variable is D_m and the parameterized PSD is valid for $T > -50^{\circ}\text{C}$. Field et al. [2005, hereinafter F05] developed a bimodal PSD based on the in-situ data (at $D_m > 100$ μm) acquired around the British Isles. It is valid for mid-latitude clouds at $T > -50^{\circ}\text{C}$. Unlike the other three studies, this parameterization has no observational constraint at $D_m < 100$ μm and therefore should be viewed with caution in the deduced T_{cir} -IWC relation since the total IWC may have a significant contribution from particles with $D_m < 100$ μm .

Because the PSD parameterizations other than the MH97 are limited to temperatures $> -50^{\circ}\text{C}$, we focus only on the error assessment at 215 hPa (or -50°C). To compare these different PSD parameterization schemes, we assume the mass-diameter relation described in Brown and Francis (1995), and convert D_m to D (mass equivalent diameter) when needed. At this level, the

modeled *Tcir*-IWC relations for H02 and DL02 have a steeper (50% and 100%, respectively) slope in the linear region than MH97, meaning that the H02 and DL02 PSDs would yield a smaller IWC by the similar percentages. The modeled slope for F05 is steeper by 200% from the MH97 *Tcir*-IWC relation, which would reduce the retrieved IWC more. These different PSD parameterizations suggest that the IWC retrieval from the MH97 PSD is likely to be too high at 215 hPa. Since both H02 and DL02 are based on tropical and subtropical clouds, the percentage differences relative to MH97 reflect uncertainty due to different parameterization schemes. Furthermore, the larger percentage difference between F05 and MH97 could result from sampling differences between mid-latitude (F05) and tropical (MH97) clouds, but the large uncertainty of F05 PSD at $D_m < 100 \mu\text{m}$ remains to be quantified. Therefore, our conservative estimate for the PSD-induced uncertainty would be 100% in the modeled *Tcir*-IWC relation.

At pressures ≤ 147 hPa, the sparsity of in-situ PSD measurements is even more severe, which could yield even larger uncertainty in the MH97 parameterization than at 215 hPa. For example, in-situ PSD measurements may be biased toward certain types of high clouds [i.e., cirrus outflows in the MH97 case], not applicable for strong deep convective clouds. To assess impacts of convection-perturbed PSDs, we conducted a sensitivity study by manipulating the temperature dependence in the MH97 parameterization. In this test, we replace the MH97 PSD parameters at -75°C with ones at -60°C , as a presumable change due to deep convection. We found that changing PSD characteristics would lead to a $\sim 30\%$ error in the modeled *Tcir*-IWC relation at -75°C . This error would be larger if the clouds were lifted from a lower altitude.

Uncertainty due to Particle Shapes

The modeled *Tcir*-IWC relation can also be affected by uncertainty about ice particle habits or shapes that make *Tcir* polarization-dependent. The MLS IWC retrieval currently neglects

polarization differences by assuming spherical particles, and here we evaluate potential errors due to this assumption. Evans and Stephens [1995] found that different particle habits may induce a factor of 2-3 differences in volume extinction coefficients compared to spherical particle results, but the differences reduce to 100% in the derived T_{cir} -IWP relation for the worst scenario (i.e., consisting of all non-spherical particles aligning in the same orientation). In reality, large ice particles in the upper troposphere are associated with strong turbulence, and these non-spherical particles are likely to orient themselves semi-randomly. Analyzing the 122 GHz T_{cir} observed by Aura MLS, Davis et al. [2005b] found that the polarization differences are generally less than 10% of the observed T_{cir} values. Using the 3D RT cloudy-sky model developed by Davis et al. [2005a], Davis et al. [2005b] found that the aspect ratio of 1.3 fit best to the observed polarization differences at 122 GHz. Using the same aspect ratio, we modeled the polarized T_{cir} differences at 240 GHz and found that they are generally less than 20% at $h_t > 10$ km for IWC < 200 mg/m³. Hence, we conclude that particle-shape-induced uncertainty in the V2.2 IWC retrieval is less than 20%.

Other Uncertainties

Mixed-phase clouds may alter the T_{cir} -IWC relation by producing more emitted than scattered radiation inside clouds. Because liquid clouds are much more (170× at 240 GHz and -30°C) efficient emitter/absorber than ice, mixing ice and liquid droplets may reduce T_{cir} sensitivity to ice as much as 10-40% at 240 GHz with liquid water content (LWC) of 10-150 mg/m³ up to a -40°C altitude. Mixed-phase clouds occur rarely at $T < -40^\circ\text{C}$ because liquid droplets would freeze spontaneously [Hogan et al., 2003]. Since most of the mixed-phase clouds are below the valid MLS IWC range, this type of error is unlikely to have significant impacts on the MLS retrieval.

Finally, MLS T retrieval error can cause large uncertainty in the derived T_{cir} . As discussed above in the T_{cir} error section, the T uncertainty (~ 3 K at 215 hPa) contributes most to the 240-GHz T_{cir} precision. As shown in Schwartz et al. [2007], the T precision exhibits significant geographical variability, and therefore, the screening method used for the V2.2 IWC data will likely produce more false detections in a noisier region within the same latitude bin. As a result, some artificial clouds with low IWC values may be found in a cloud map. These artificial clouds usually occur at wintertime high latitudes where stratospheric gravity waves (GWs) cause increased error in MLS T retrieval. The GW-induced T error is reduced substantially in the V2.2 retrieval, which improves cloud detection at high latitudes.

Summary of Systematic Uncertainties

Systematic uncertainties of the V2.2 IWC are summarized in Table 3. Although cloud inhomogeneity can cause large uncertainties on individual IWC measurements, this error is nearly random and can be reduced by averaging the data. The inhomogeneity-induced error will be corrected properly in the future with a 2-D tomographic IWC retrieval. The largest non-random uncertainty in the V2.2 IWC retrieval is from the PSD assumptions used in the cloudy-sky RT models. The MH97 parameterization used for the V2.2 IWC retrieval may not be applicable to deep convective cores nor to mid-latitude clouds. The modeled T_{cir} -IWC relations from different PSDs can differ systematically by as much as 100% at 215 hPa. Currently, we do not have a PSD parameterization that can represent global ice cloud properties accurately. In-situ observations of PSDs remain very sparse and incomplete, resulting in poorly-constrained microphysical assumptions used in MLS IWC retrievals. Much work is needed to improve PSD parameterization and statistical properties of global ice clouds.

Table 3. Estimated Systematic Uncertainties for MLS V2.2 IWC

<i>P_{tan}</i> (hPa)	CI r.m.s. Uncertainty ^a		CI Scaling Uncertainty ^b		MH97 Fitting	Other PSDs ^c	Ice Habits	Mixed Phase
	0.5-5 K	5-20K	Trop.	ExtraTrop				
83	50%	-	-50%	-	< 30%	-	< 20%	-
100	50%	40%	-70%	-40%	< 30%	-	< 20%	-
121	100%	70%	-20%	+20 %	< 30%	-	< 20%	-
147	100%	80%	-30%	-20 %	< 30%	-	< 20%	-
177	150%	80%	+20%	-30 %	< 30%	-	< 20%	-
215	300%	80%	+80%	-40 %	< 30%	100%	< 20%	< 40%

a) These are 2σ r.m.s (root mean square) errors on a single IWC measurement due to cloud inhomogeneity (CI). They are estimated from the simulated results in Figure 11 and reported for two ranges of T_{cir} values.

5 b) CI-induced scaling errors in the V2.2 T_{cir} -IWC relations are strongly latitude-dependent. They are estimated separately for the tropical and extratropical bins as defined in Figure 11.

c) This is uncertainty due to PSD parameterizations other than MH97.

4 Comparisons with AIRS, OMI, and MODIS

In this section we compare MLS cloud fraction (CFR) and cloud top pressure (CTP) with those observed by AIRS, OMI and MODIS. In the AIRS and OMI comparisons we define MLS CFR as the ratio of the number of cloudy measurements over the total number of samples, and MLS CTP as the lowest pressure level in each profile at which a cloud is detected.

4.1 Comparison with AIRS

For AIRS comparisons we focus on monthly cloud statistics in January and June 2005. The AIRS data used for this study are version 4.0 level 3 (L3) CFR and CTP [Olsen et al., 2005], which are assembled from the AIRS level 2 (L2) [Harris et al., 2005] products. The AIRS L3 data file contains geophysical parameters on a $1^\circ \times 1^\circ$ latitude-longitude grid. Although the AIRS cloud data products have been validated for latitudes between 50°S and 50°N , the CFR and CTP data are only validated over the ocean. As noted in Olsen et al. [2005], AIRS cloud observations over land or icy/snowy surfaces might contain a large uncertainty. Other known caveats include:

(1) AIRS cloud retrievals at altitudes higher than ~ 150 hPa are relatively poor due to weaker signal-to-noise ratio; (2) The AIRS retrieval puts a cloud top at the tropopause if it occurs above

it. Because MLS V2.2 data have not been completely processed for these months, we use V1.5 IWC data in the MLS-AIRS comparisons. The MLS CFR in a given region is defined as the number of $IWC > \mu + 3\sigma$ divided by total number of samples.

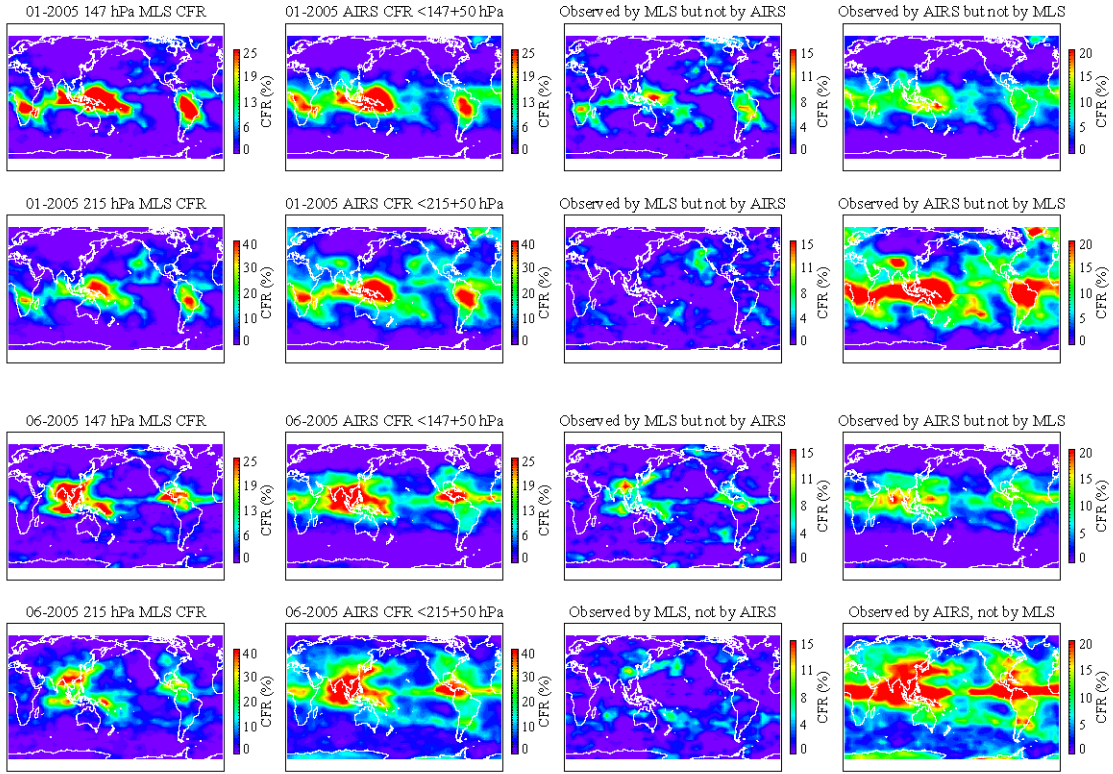


Figure 13 Maps (from left to right) of MLS CFR, AIRS CFR, AIRS-missed CFR (observed by MLS but not by AIRS), and MLS-missed CFR (observed by AIRS but not by MLS) for January 2005 (upper two rows) and June 2005 (lower two rows) at 147 and 215 hPa. The maps are averaged from daily collocated MLS and AIRS measurements. A 50 hPa offset is used in subsetting AIRS CFR to account for MLS FOV effects. Surface contamination is clearly seen in AIRS CFR over the Antarctic.

For MLS and AIRS CFR comparisons, we first collocate all cloud measurements by interpolating the AIRS data onto each MLS measurement location. The AIRS CFRs are averaged into a grid box of $2^\circ \times 1^\circ$ (along \times cross track), centered on the MLS data point. We use the lowest CTP value in each box as the representative cloud pressure because the averaged CTP would induce a large bias in the cases of broken clouds. To compare AIRS and MLS CFRs at different MLS pressure levels, we screen the AIRS CFRs to include those with the associated

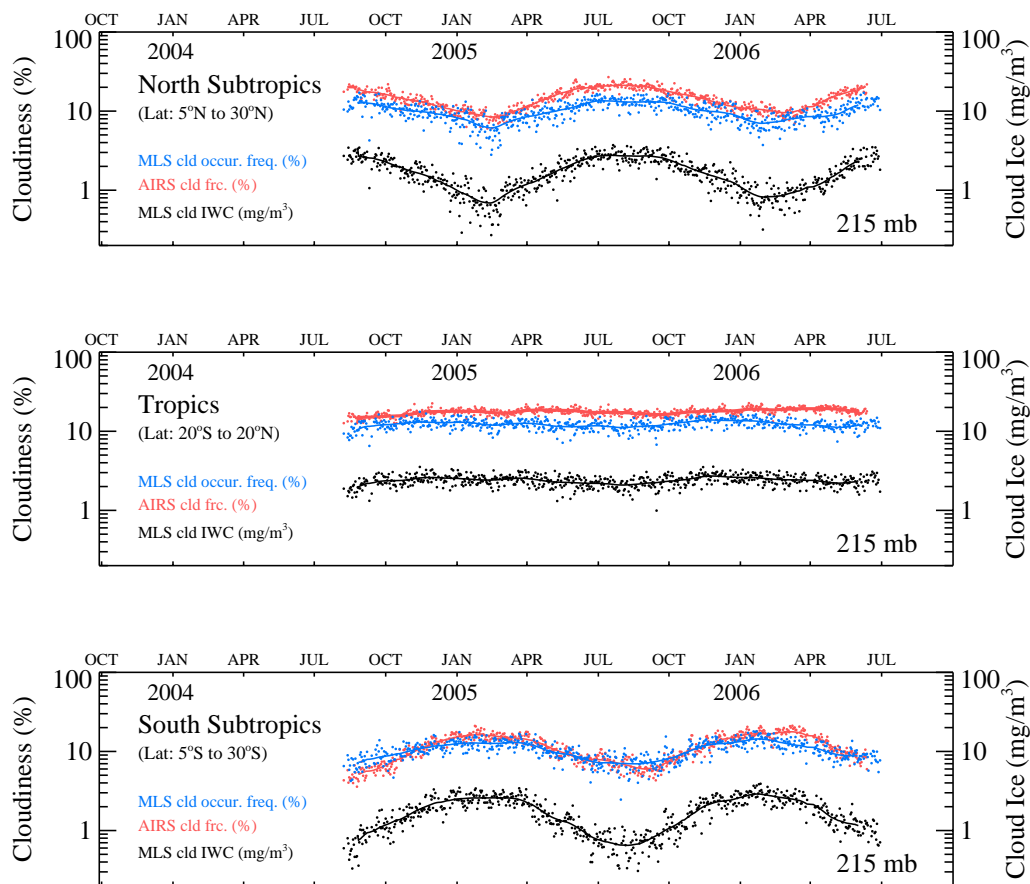
CTP equal or less than the MLS CTP plus a 50 hPa offset. This offset is introduced to account for MLS vertical FOV effects.

Figure 13 compares monthly mean CFR maps from MLS and AIRS for January and June 2005 at 215 and 147 hPa. These are based on the daily collocated observations as described above and averaged to a $4^{\circ} \times 8^{\circ}$ latitude-longitude grid. Overall MLS and AIRS CFR morphology show good agreement and AIRS CFR may be slightly higher than MLS on average. Because AIRS has a better sensitivity than MLS to cloud scattering, higher AIRS CFR is expected and the MLS-missed CFR has a wider latitudinal distribution than MLS CFR.

The cases important to the MLS validation are the AIRS-missed CFRs. At 147 hPa, the MLS-missed CFRs in both months have a morphology similar to MLS CFR at this pressure. We investigate them further by changing cutoff pressure threshold to include more AIRS clouds from a lower altitude. We find that the AIRS-missed cases gradually disappear if more low-altitude clouds are included, suggesting that AIRS CTP likely has a high pressure bias or a low bias in cloud top height at the 147 hPa pressure level. This conclusion is consistent with other comparative studies that indicate an AIRS systematic error in CTP [e.g., Sherwood et al., 2004; Kahn et al., 2005]. At 215 hPa the AIRS-missed CFR are mostly found at mid and high latitudes where the CO₂ cloud slicing technique used by AIRS may have difficulty in dealing with complicated temperature profiles. Therefore, the AIRS-missed cases at this pressure could result from AIRS sensitivity error.

Figure 14 shows the time-series of daily mean MLS IWC/CFR and AIRS CFR at 215 hPa from August 2004 to June 2006 for the tropics (20°S - 20°N), northern (5°N - 30°N), and southern (5°S - 30°S) subtropics. AIRS shows a generally larger CFR than MLS, as expected for its better sensitivity to cloud scattering. However, the CFR difference is reduced significantly and even

reversed in the southern subtropics during some periods of time. As discussed above, AIRS CTP error can cause such a mismatch in CFR by placing clouds at a lower altitude. In all cases, the observed IWC and CFR exhibit a similar annual cycle.



5 Figure 14 Time-series of MLS and AIRS daily averages for north sub-tropics (top-panel), tropics (mid-panel) or south sub-tropics (lower-panel). The solid lines are the monthly running means on the daily values. AIRS CFR (%), MLS IWC (mg/m^3) and MLS CFR (%) are colored in red, black and blue, respectively.

In summary, MLS and AIRS CFRs exhibit similar morphologies at 147 and 215 hPa for January and July 2005 with a pressure offset of 50 hPa. At 147 hPa the AIRS-missed (detected
10 by MLS but not by AIRS) clouds suggest a low bias in AIRS cloud top height. Comparisons of

MLS and AIRS CFR time series show that the data sets track to each other closely over seasonal cycles, but AIRS CFR reveals a slightly larger amplitude in subtropical seasonal variations than MLS CFR. Hemispheric differences in the subtropics are also larger in AIRS CFR.

4.2 Comparison with OMI

Two retrieval techniques have been used in deriving OMI cloud products, which are named OMICLDO2 and OMICLDRR, corresponding to techniques based on the O₂-O₂ 477 nm absorption [Acarreta *et al.* 2004] and the 355-365 nm rotational Raman scattering by N₂/O₂ [Joiner *et al.*, 2006], respectively. In this study, we limit our study to the comparison with the
5 collection 002 OMICLDO2 products.

The OMICLDO2 retrieval estimates the column of air above cloud layers using the strength of the O₂-O₂ absorption feature at 477 nm in reflected sunlight. An effective CFR and cloud pressure (CP) are determined for each pixel [Acarreta *et al.* 2004]. Unlike geometric CFR defined in MLS and AIRS, the OMI CFR is adjusted to best fit the reflectance at the top of
10 atmosphere by assuming a fixed (0.8) cloud albedo. Hence, some cirrus clouds are likely missed or underestimated under this assumption, producing a low effective CFR. In this retrieval model, the surface albedo comes from climatology and include a Rayleigh scattering correction. Simulations showed that the retrieved CP is not CTP. Instead it represents a mid-level height of the cloud layer and the difference between OMI CP and correlative CTP observations can be as
15 large as 300 hPa on average [Sneep *et al.*, 2007]. Therefore, a larger pressure offset is expected for the MLS-OMI comparison than for the MLS-AIRS comparison. In addition, the MLS-OMI comparisons are limited to only daytime observations. In this study, we compare MLS V1.5 IWC data with OMI CFR selected by OMI CP for January and July 2006.

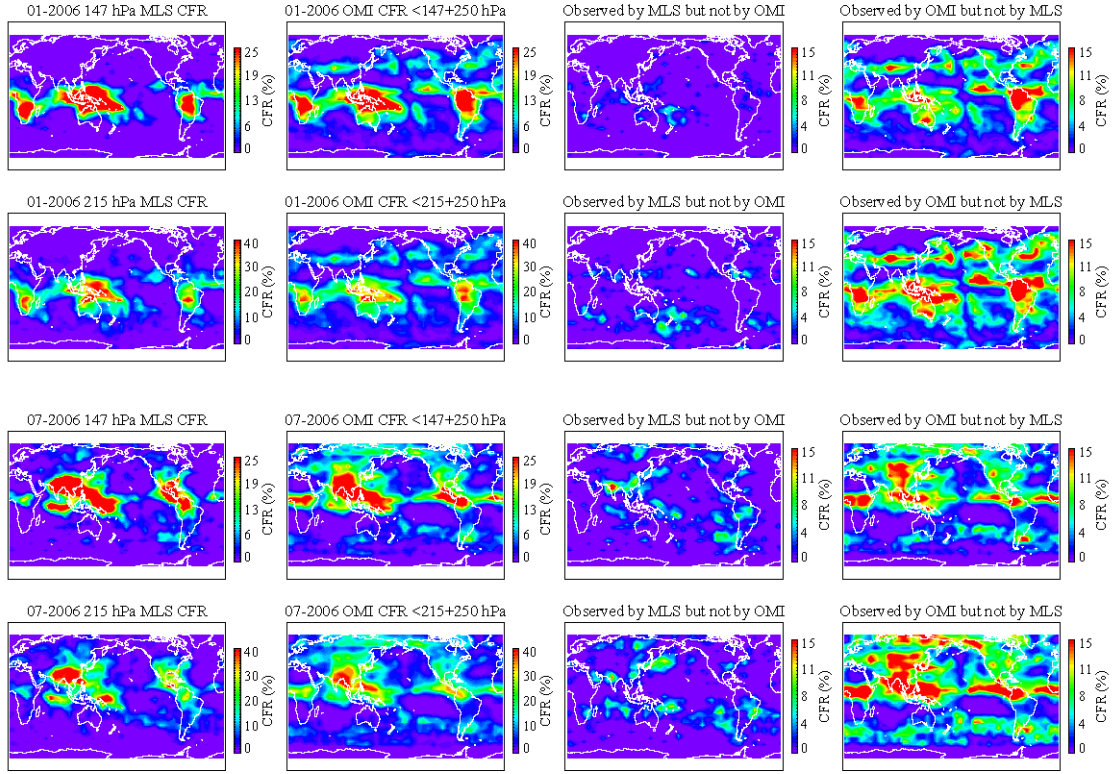


Figure 15 Maps (left-to-right) of MLS CFR, OMI CFR, OMI-missed (observed by MLS but not by OMI) CFR, and MLS-missed (observed by OMI but not by MLS) for January 2006 (upper two rows) and July 2006 (lower two rows) at 147 and 215 hPa. The maps are averaged from daytime collocated MLS and OMI measurements. The 250 hPa offset is used in calculating OMI CFR to account for OMI CP biases and MLS FOV effects.

As in the comparisons with AIRS data, OMI cloud data are collocated and averaged according to MLS measurement locations. To compare OMI CFR with MLS CFR at different MLS P_{tan} , we select the OMI CFR with the criterion: $OMP\ CP < (MLS\ P_{tan} + \text{offset})$. We calculate the OMI CFRs sampled by MLS using three different pressure offsets: 50, 150, and 250 hPa, to account for the OMICLDO2 CP bias and MLS FOV effects. Only the results for the 250 hPa offset are shown here because but there are large MLS-OMI biases are in the 50 and 150 hPa offset cases.

Figure 15 compares the 147 and 215 hPa monthly morphologies of MLS and OMI CFR, as well as the OMI-missed cases (observed by MLS but not by OMI), for January and July 2006. With the 250 hPa offset adjustment, the monthly MLS and OMI morphologies agree well. The

maps show that the adjusted OMI CFR still has generally low biases against MLS CFR at 147 and 215 hPa. The OMI CFR maps from the adjusted CP reveal wintertime cloud activity in a narrow mid-latitude band, which is not seen by AIRS. The MLS-missed clouds show overall larger percentages in July than in January. As in the MLS-AIRS comparison, the distributions of the OMI-missed clouds at 215 hPa spread broadly to mid and high latitudes.

In summary, MLS and OMI CFRs show overall good agreement in global morphology at 147 and 215 hPa after OMI CP is offset by 250 hPa. Such an offset is consistent with the finding in the OMI-MODIS comparison [Sneep et al., 2007]. The OMI and AIRS CFR maps show some significant differences at 147 and 215 hPa, where many OMI clouds at wintertime mid-latitudes are not seen by AIRS.

4.3 Comparison with MODIS

MODIS uses the CO₂ slicing technique to retrieve CTP with precision between 50 and 150 hPa [Frey et al., 1999]. The MODIS data used here are the MYD06_L2 cloud top product, and MLS V2.2 CTP is simply defined as the lowest pressure at which the IWC exceeds 0.7 mg/m³.

For the case shown in Figure 16(a-b), we compare MLS and MODIS CTP for a small set of collocated measurements. the A-train passed over a cloudy region near the equator at 125°W on 20 April 2005. During 21.94-21.99 UTC, MLS observed significant IWC at pressures -2.4 and -2.2, which corresponds to low MODIS CTP consistently. Earlier around 21.90 UTC, some scattered cirrus with top mostly below 261 hPa level are not detected by MLS IWC, which is below the range of MLS IWC validity.

For a more extensive MLS-MODIS comparison, we first collocated the MODIS data by assigning a 15 × 200 km (3 × 41 pixels) strip along the MLS track, centered on each MLS tangent point. We tagged each MODIS CTP with the standard deviation of CTP to indicate the degree of

cloud top inhomogeneity within the strip. The MODIS CTP used to compare with MLS is the average in each strip. The MLS V2.2 CTP is simply defined as the lowest pressure at which the IWC exceeds 0.7 mg/m^3 .

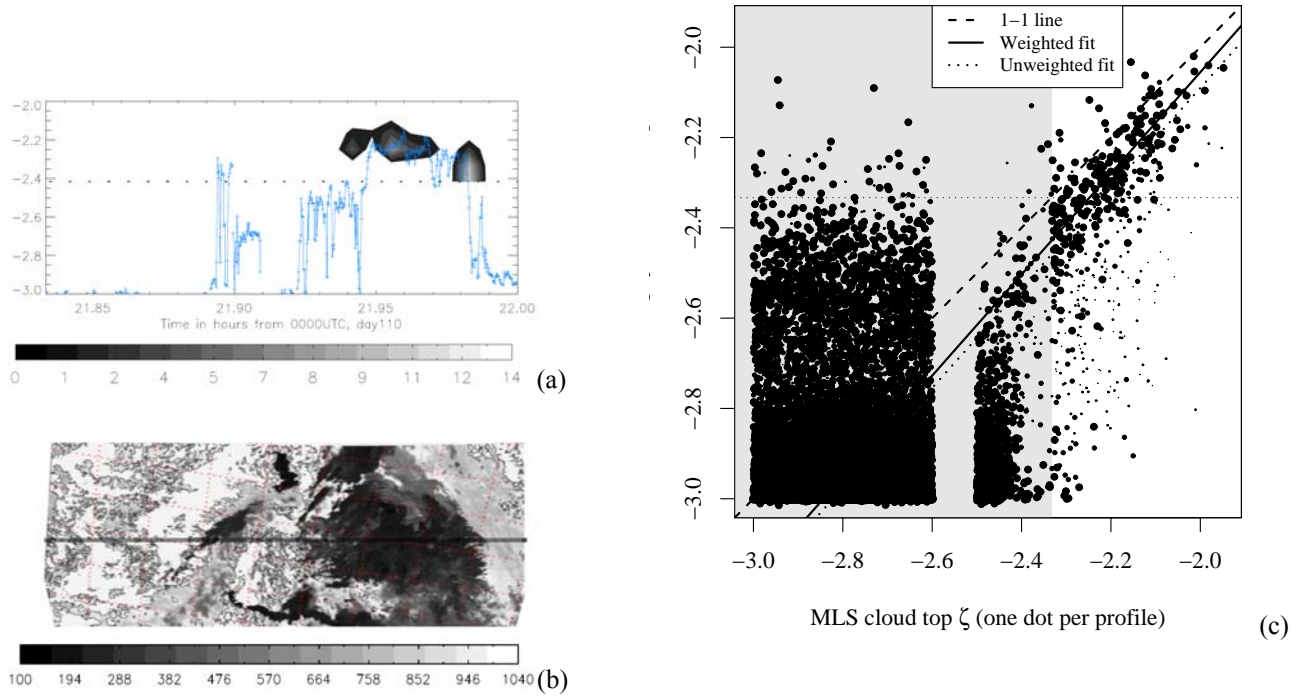


Figure 16 (a) MODIS CTP and MLS IWC from 21.50 – 21.55 UTC, on 25 April 2005. MODIS CTP is represented by the grey line. MLS IWC in mg/m^3 is shown as the shaded area. MODIS CTP is indicated by the grey line and defined as $\zeta = -\log_{10}(P/\text{hPa})$. (b) MODIS CTP granule in hPa over the [137W, 110W, 15S, 19N] region. The faint strip on image represents the MLS measurement pass. (c) Comparison of MLS and MODIS CTP in ζ unit for the period of 14-16 October 2005. The MODIS values are the mean of a 3×41 pixel region centered on the nominal MLS measurement position. The size of the dots indicates the uniformity of the MODIS clouds: the smallest dots have the largest standard deviation of CTP. MLS does not report IWC at pressures higher than 316 hPa. In the plot, such points are assigned a cloud top height randomly between $\zeta = -3.0$ and $\zeta = -2.6$, to allow some impression to be obtained of the density of points. The MLS data are reliable only in the unshaded region, where the pressure is less than 215 hPa ($\zeta > -2.33$).

Figure 16(c) compares MODIS and MLS CTPs acquired during 14-16 October 2005. The vast majority of MLS profiles have no measurable IWC in this ensemble. For most of these profiles the coincident MODIS CTP is > 215 hPa although there are a small number of cases where MODIS observes a high cloud and MLS does not. Where MLS observes a cloud at pressures lower than 215 hPa, MODIS nearly always observes clouds as well. If comparison is restricted to cases where the MODIS clouds are rather uniform over the MLS footprint (small CTP standard deviations or large

dots in Figure 16), a positive correlation between MLS and MODIS CTP emerges, with the slope of a linear fit to the data being rather close to 1. The linear fits shown in the plot use all points where the MLS CTP is smaller than 215 hPa ($\zeta > -2.33$) and the MODIS CTP is smaller than 630 hPa ($\zeta > 2.8$). For the solid line, the points are weighted by the inverse of the variance in the MODIS data.

5 There is an offset of ~ 1.5 km with MLS cloud height being higher, the size of this offset is dependent on the definition chosen for the MLS CTP. For regions with broken clouds (small dots in Figure 16c) the MODIS CTP is usually much smaller than the MLS CTP because MLS is detecting the highest clouds in a region which also contains pixels with low cloud.

In summary, the agreement between the two instruments is good considering their very different viewing geometries. At CTPs < 215 hPa, the correlation between MLS and MODIS CTPs exhibits a slope of ~ 1 and MLS cloud height is slightly higher by ~ 1.5 km.

5 Comparisons with CloudSat

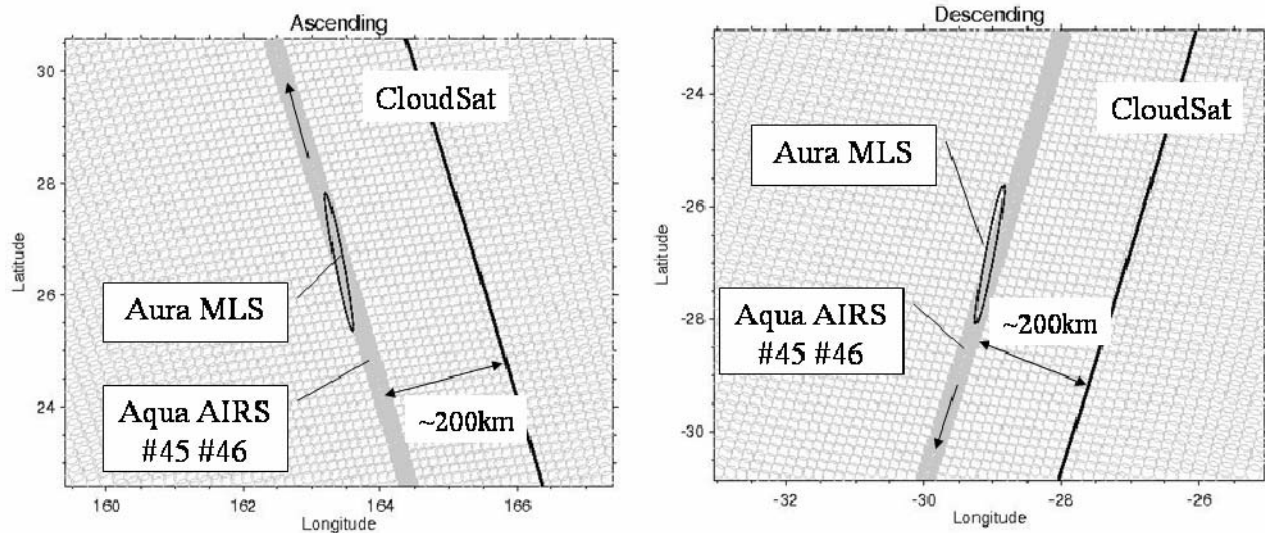
CloudSat is the first spaceborne 94-GHz cloud profiling radar (CPR) that measures vertical structures of clouds and precipitation [Stephens et al. 2002]. It was launched in April 2006 and currently flies in formation with Aqua, Aura, and CALIPSO satellites as a part of the NASA A-Train. However, the MLS and CloudSat sampling tracks are separated by ~ 200 km in most parts of the orbit [Figure 17]. This sampling offset makes it difficult to compare MLS and CloudSat IWC measurements directly on a point-by-point basis. In addition, MLS and CloudSat measurements are also separated in time by 7-8 min, which marginally qualifies as “coincident” cloud measurements.

20 Coincident cloud measurements must be taken in a time period shorter than cloud temporal variability. For example, deep convective systems can raise cloud heights by ~ 4 km in 7 minutes with a 10 m/s updraft (Geerts et al., 2000). Given these sampling differences, we choose to compare statistical properties of MLS and CloudSat IWC measurements.

IWC is a bulk cloud property averaged for a given volume when it is measured by different instruments. Because of large cloud inhomogeneity, IWC statistics can be different if the IWC measurement volumes are different. For IWC comparisons, one needs to first average the finer-resolution data to match the low-resolution data in terms of measurement volume. A CloudSat IWC profile has vertical resolution of 240 m and horizontal resolutions of ~ 1.4 km (cross-track) by 1.8 km (along-track) with the along-track sampling of every 1 km. To compare with MLS, we average CloudSat IWC profiles to match the MLS measurement volume along track. Using the rectangular box defined in Figure 4, we average CloudSat IWC for CloudSat-MLS comparisons, but neglect effects of cross-track averaging.

The official CloudSat 2B-IWC retrieval technique is described by Austin and Stephens [2001], in which a spectral width for Gamma PSD is retrieved along with IWC. The 2B-IWC retrieval is limited to daytime because it uses radar reflectivity from CloudSat and visible optical depth from MODIS. In addition, a radar-only retrieval is also developed by the CloudSat team, called 2B-IWC-RO, which can produce IWC profiles for both day and night. The current 2B-IWC-RO algorithm fits a single spectral width to each radar reflectivity profile, which means that the Gamma distribution shape is same in the entire profile. In this study we use the recently released (Release 3) 2B-IWC-RO data, in which IWC is zeroed for temperatures above 0°C and scaled linearly to zero for temperatures between -20°C to 0°C . This product applies a reflectivity threshold for cloud detection before the IWC retrieval, and therefore the IWC statistics below the reflectivity threshold (equivalent to $\sim 5 \text{ mg/m}^3$ in IWC) is not useful. The reflectivity threshold yields incomplete IWC statistics by eliminating noise statistics for $\text{IWC} < 5 \text{ mg/m}^3$. This truncation apparently affects the MLS-CloudSat IWC comparison since it requires to average some 3200 CloudSat measurements inside each MLS-volume box. If CloudSat IWC noise statistics were fully preserved, we could trust

the averaged CloudSat IWC down to $5/\sqrt{3200}$ or $\sim 0.1 \text{ mg/m}^3$. Because CloudSat IWC noise statistics are incomplete, we should view the results of the averaged CloudSat IWC with caution when the average IWC values $< 5 \text{ mg/m}^3$.



5 Figure 17 Diagram of MLS, AIRS, and CloudSat sampling tracks as shown under the A-Train configuration on 4 August 2006. In this configuration CloudSat is flying in formation with CALIPSO lidar and the latter needs to point slightly off nadir to avoid sun glints, which results in CloudSat footprints $\sim 200 \text{ km}$ off from the Aqua nadir (#45 and #46) or the Aura MLS tangent footprint (long ellipse) at most latitudes.

To compare MLS and CloudSat IWC statistics, we generate normalized PDFs for January and
 10 July at five latitude and six altitude bins. All PDFs are normalized such that the integrated PDF is equal to unity. For MLS V2.2 IWC, we use all the data that have been processed to date for these months in 2005-2007 to improve the statistics. Since interannual variations of IWC PDFs are relatively small ($< 20\%$) based on MLS V1.5 observations, the multi-year monthly statistics can be used to characterize overall MLS-CloudSat IWC differences. The PDF method has been used in a
 15 number of cloud ice studies [e.g., Mace et al., 2001; Hogan and Illingworth, 2003; van Zadelhoff et al., 2004], and also suggested for tracer gas comparisons in the case where coincident measurements are difficult to obtain [Lary and Lait, 2006]. One of the advantages with the PDF method is to allow comparisons of noise, sensitivity, and accuracy collectively. These data

attributes are usually mixed together after IWC is averaged and become difficult to quantify individually by comparing the averages (e.g., monthly maps).

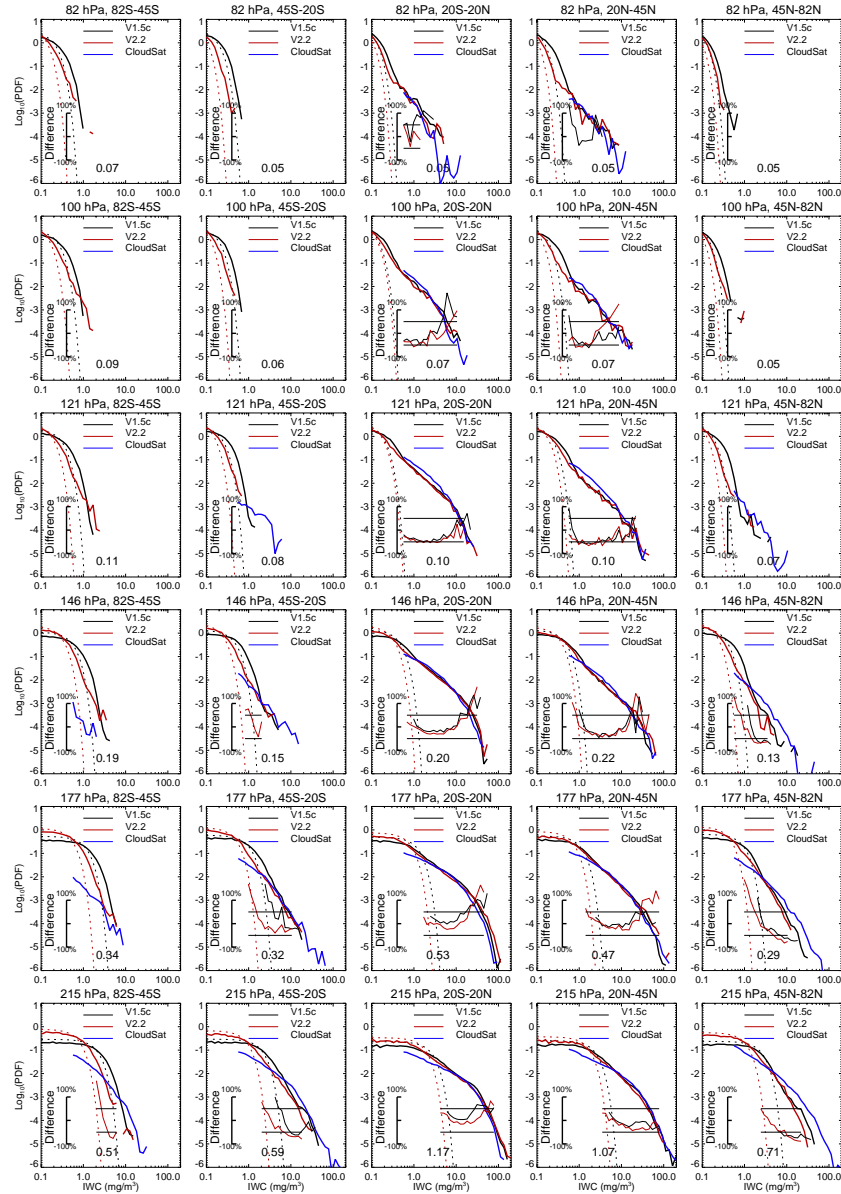


Figure 18. Comparisons of MLS V1.5c, V2.2, and CloudSat IWC PDFs for July at different latitude bins and pressure levels. Dotted lines are the distributions of estimated Gaussian noise for MLS IWC and the estimated standard deviation σ of V2.2 IWC noise is given in each panel. The rising PDFs at $IWC < 3\sigma$ are mostly contributed by noise. CloudSat IWC PDFs below 5 mg/m^3 should be viewed with caution because of its incomplete noise statistics (see text). Percentage differences of MLS V1.5c and V2.2 PDFs with respect to CloudSat (MLS-CloudSat) are plotted under the PDFs for the range of $3\sigma < IWC < 80 \text{ mg/m}^3$, and the horizontal lines indicate $\pm 50\%$. In addition, only PDF differences with significant statistics (i.e., number of samples in an IWC bin > 4) are shown. MLS V1.5c statistics are based on 60 days of data in 2005-2007, V2.2 on 29 days of data in 2006, while CloudSat statistics are from 31 days of data in 2006.

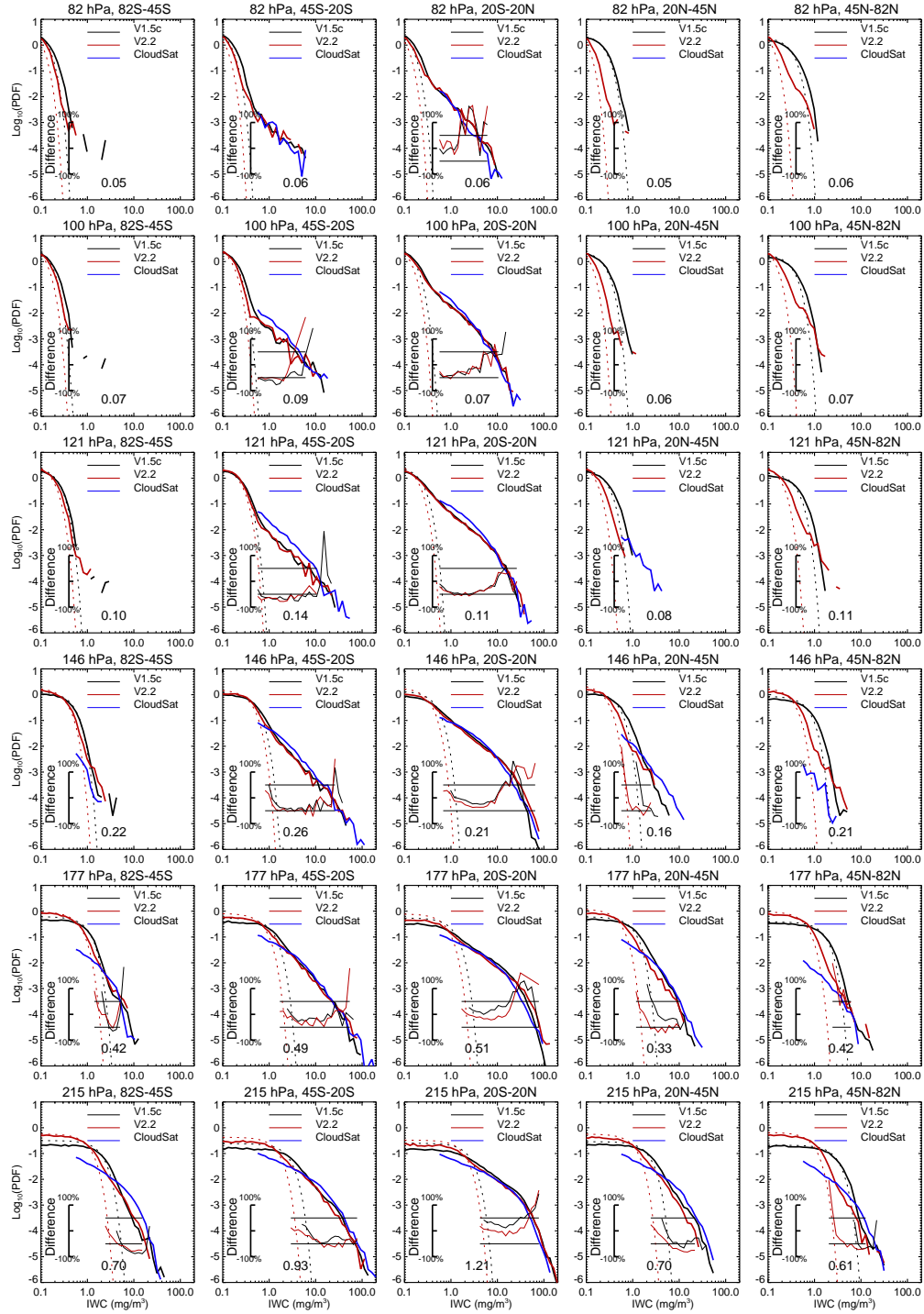


Figure 19. As in Figure 18 but for January. MLS V1.5c and V2.2 statistics contain respectively 89 and 36 days of data from 2005-2007 while CloudSat statistics are from 29 days of data in 2007.

Figures 18-19 compare monthly PDFs for measurement noise, sensitivity, and accuracy of MLS and CloudSat IWC retrievals. MLS and CloudSat PDFs generally agree and track well, showing consistency over a wide range of IWC values for most latitude and pressure bins. The percentage differences, similar in both V1.5c and V2.2 data, are generally less than 50% in the valid IWC ranges.

In the tropical bins where $IWC < 5 \text{ mg/m}^3$, MLS IWC is lower than CloudSat by $\sim 50\%$ at 100 and 121 hPa. This is consistent with the inhomogeneity-induced error in Figure 11 where we estimated the inhomogeneity-induced scaling error to be -20% and -70% in the tropics. In other words, the MLS-CloudSat differences would be reduced if MLS corrected its inhomogeneity error. The biases at 215-147 hPa are relatively small for $IWC < 10 \text{ mg/m}^3$. If we include the inhomogeneity-induced scaling error in MLS V2.2 IWC, the MLS-CloudSat differences could be as large as 80%. All MLS-CloudSat biases tend to increase with IWC from negative to positive, which is consistent with the behavior of the V2.2 scaling error due to cloud inhomogeneity [Figure 11]. The V2.2 T_{cir} -IWC relations deviate more from the simulated relations at larger IWC values, showing that V2.2 tends to overestimate IWC at 147 and 177 hPa for values $> 10 \text{ mg/m}^3$.

In the mid- and high-latitude bins, larger error rises at the small IWC values (close to MLS 3σ noise), suggesting a possibly increased false alarm rate if the 3σ criterion is used for cloud detection. Because MLS IWC noise can be non-Gaussian (i.e., with a wider distribution at larger IWC values), the 3σ detection will introduce more false detections at these latitudes. In all pressure bins, the V2.2 noise is smaller than V1.5 noise.

In high latitude bins (45°N - 90°N in July or 45°S - 90°S in January), MLS IWC exhibits a low ($\sim 70\%$) bias against CloudSat at 215-177 hPa for $IWC > 5 \text{ mg/m}^3$. This low bias is consistent with the V2.2 retrieval model error revealed in Figure 11 under a realistic environment of cloud

inhomogeneity. Figure 11 shows that the V2.2 IWC retrieval may be biased -40% low in the extratropics and the bias may increase with IWC. However, as discussed in section 3.3, the V2.2 IWC retrievals may have a high bias due to the MH97 PSD used by the retrieval. The CloudSat retrieval assumes a single-mode Gamma PSD, which may oversimplify cloud PSDs in this region [e.g., Korolev et al., 2001; Delanoë et al, 2005]. Therefore, the uncertainty in high-latitude IWC retrievals remains quite large at present. It is unclear what causes the MLS-CloudSat IWC differences at high latitudes. A more accurate PSD parameterization will be helpful, which can be obtained through future validation field campaigns in this data-sparse region.

6 Conclusions and Future Work

The MLS V2.2 algorithm produces IWC profiles that are scientifically useful at pressures between 261 and 83 hPa. The user needs to screen the IWC data on a daily basis to remove bias and obtain measurement precision with the method described in section 2.5. In this study we have described and validated MLS V2.2 IWC retrievals at 215-83 hPa through model simulations and comparisons with other correlative datasets. The V2.2 IWC precision, accuracy, and resolution are assessed and the results are summarized in Table 4.

Table 4. Summary of estimated MLS V2.2 IWC precision, accuracy, and resolution

Pressure (hPa)	Typical Precision ^a (mg/m ³)	Accuracy ^b (%)		Resolution ^c H × H _⊥ × V (km)	Valid IWC Range ^d (mg/m ³)
		<10 mg/m ³	>10 mg/m ³		
83	0.06	100%	-	200 × 7 × 5	0.02 - 50
100	0.07	100%	100%	200 × 7 × 5	0.02 - 50
121	0.1	100%	100%	250 × 7 × 4	0.04 - 50
147	0.2	100%	100%	300 × 7 × 4	0.1 - 50
177	0.3-0.6	150%	100%	300 × 7 × 4	0.3 - 50
215	0.6-1.3	300%	100%	300 × 7 × 4	0.6 - 50

a) These are typical 1σ precisions of single IWC measurements where the better values are for the extratropics and the poorer values for the tropics. The precision for a particular measurement must be evaluated on a daily basis using the method described in the text.

b) Estimated from the V2.2 IWC retrieval uncertainties due to cloud inhomogeneity, modeled *Tcir*-IWC relations, and PSD parameterizations.

c) $H_{||}$, H_{\perp} and V denote, respectively, the along-track, cross-track and vertical extent of the atmospheric volume sampled by an individual MLS measurement.

5 d) This is the range where the stated precision, accuracy and resolution are applied. IWC values above this range, currently giving qualitative information on cloud ice, require further validation for quantitative interpretation.

The V2.2 IWC measurements represent a volume-averaged quantity of which the volume size can be approximated with a rectangular box in the vertical and along-track directions as shown in

10 Figure 4. The dimensions of these rectangular boxes are defined as the vertical and along-track horizontal resolutions of the V2.2 IWC measurements, which are given in Table 4. The V2.2 IWC measurements generally have better precision at low pressures and at high latitudes than in other regions, and is improved significantly over the V1.5 data, especially at high latitudes. Cloud inhomogeneity and PSD assumption contribute the largest uncertainties to the V2.2 IWC retrieval.

15 Most of the inhomogeneity-induced uncertainties can be reduced through averaging (e.g., in monthly maps) since cloud inhomogeneity generally induces random errors in the V2.2 IWC. However, inhomogeneity-induced scaling errors in the V2.2 IWC retrieval, ranging from -70% to +80%, can not be reduced by averaging. The inhomogeneity-induced uncertainty is larger at higher pressures and for smaller IWC values. In this study, the validation of V2.2 IWC is limited to the

20 measurements $< 50 \text{ mg/m}^3$ where the *Tcir*-IWC relations are nearly linear. The IWC measurements at values $> 50 \text{ mg/m}^3$ are still scientifically useful but only in a qualitative sense.

Comparisons with AIRS, OMI, MODIS show that MLS cloud top heights are slightly higher by $\sim 1.5 \text{ km}$, part of which can be caused by MLS vertical FOV effects. AIRS and OMI cloud heights likely have a low bias in the upper troposphere. Comparisons with CloudSat for months of January

25 and July show that MLS V2.2 and CloudSat IWC retrievals agree generally well with the PDF differences $< 50\%$ in the overlapped sensitivity range. At pressures $< 177 \text{ hPa}$ and extratropical

latitudes, MLS IWC has a slightly low bias compared to CloudSat, part of which can be attributed to systematic errors associated with the V2.2 IWC retrieval. However, the assumptions about the PSD used in these IWC retrievals remain as one of the largest uncertainties and needs to be reduced through future validation campaigns.

5 The V2.2 algorithm is one of the initial attempts to retrieve upper-tropospheric IWC from Aura MLS radiance measurements. It uses the simple T_{cir} -IWC relations derived from the 1-D geometry, which are affected largely by uncertainties due to cloud inhomogeneity. Most of these uncertainties can be reduced substantially with a 2-D tomographic retrieval and with the extended 2-D RT model described in section 2.2. This new IWC retrieval system is currently being developed by the MLS
10 team for 190-240 GHz channels as well as for 640 GHz channels. At the higher frequencies, MLS T_{cir} has better sensitivity to cloud scattering from small ice crystals [Wu et al., 2006], and therefore the new IWC retrievals at 240 and 640 GHz can provide bulk information on particle sizes of upper-tropospheric clouds.

Acknowledgments

15 This work was performed at the Jet Propulsion Laboratory, California Institute of Technology, under contract with the National Aeronautics and Space Administration (NASA). We thank MLS, AIRS, CloudSat, MODIS, and OMI teams for successful instrument operation and data processing, and for providing their data in this study. Discussions with Drs. G. McFarquhar and A. Heymsfield on PSD parameterization, S. Tanelli, S. Durden and G. Mace on CloudSat data, J. Joiner and A.
20 Vassikov on OMI cloud retrievals are acknowledged.

References

Acarreta, J. R., J. F. de Haan, and P. Stammes, Cloud pressure retrieval using the O₂-O₂ absorption band at 477 nm, *J. Geophys. Res.*, **109**, D05204, doi:10.1029/2003JD003915, 2004.

- Austin, R. T., and G. L. Stephens, Retrieval of stratus cloud microphysical parameters using millimeter-wave radar and visible optical depth in preparation for CloudSat. 1. Algorithm formulation. *J. Geophys. Res.*, **106**, 28,233-28,242, 2001.
- Brown, P. R. A., and P. N. Francis, Improved measurements of the ice water content in cirrus using a total-water probe. *J. Atmos. Oceanic Technol.*, **12**, 410–414, 1995.
- Cofield, R.E., and P.C. Stek, Design and field-of-view calibration of 114-660 GHz optics of the Earth Observing System Microwave Limb Sounder, *IEEE Trans. Geosci. Remote Sensing* **44**, no. **5**, 1166-1181, May 2006.
- Comstock, J. M., et al., An intercomparison of microphysical retrieval algorithms for upper-tropospheric ice clouds. *Bull. Am. Meteorol. Soc.*, **88**, 191-204, 2007.
- Davis, C. P., C. Emde, and R. S. Harwood, “A 3D Polarized Reversed Monte Carlo Radiative Transfer Model for mm and sub-mm Passive Remote Sensing in Cloudy Atmospheres,” *IEEE Trans. Geosci. Remote Sensing*, MicroRad'04 Special Issue, vol. 43 (5), pp. 1096-1101, 2005a.
- Davis, C. P., D. L. Wu, C. Emde, J. H. Jiang, R. E. Cofield, and R. S. Harwood, “Cirrus Induced Polarization in 122 GHz Aura Microwave Limb Sounder Radiances,” *Geophys. Res. Lett.*, vol. **32**, no. 14, L14806, doi:10.1029/2005GL022681, 2005b.
- Davis, C. P., H. C. Pumphrey, K. F. Evans, S. Buehler, and D. L. Wu, 3D polarised simulations of space-borne passive mm/sub-mm midlatitude cirrus observations: A case study. *Atmos. Chem. Phys. Discuss.*, in press, 2007.
- Delanoë, J., et al., Statistical properties of the normalized ice particle size distribution, *J. Geophys. Res.*, **110**, D10201, doi:10.1029/2004JD005405, 2005.
- Eriksson, P., M. Ekström, B. Rydberg, and D. P. Murtagh, First Odin sub-mm retrievals in the tropical upper troposphere: ice cloud properties, *Atmos. Chem. Phys.*, **7**, 471-482, 2007.
- Evans, K. F., and G. L. Stephens, Microwave radiative transfer through clouds composed of realistically shaped ice crystals. Part II: Remote sensing of ice clouds. *J. Atmos. Sci.*, **52**, 2058-2072, 1995.
- Evans, K. F., et al., Modeling of submillimeter passive remote sensing of cirrus clouds. *J. Appl. Meteor.*, **37**, 184-205, 1998.
- Evans, K. F., J. R. Wang, P. E. Racette, G. M. Heymsfield, and L. Li , Ice cloud retrievals and analysis with the compact scanning submillimeter imaging radiometer and the cloud radar system during CRYSTAL FACE, *J. Appl. Meteorol.*, **44**, 839–859, 2005.
- Fleming, E. L., S. Chandra, M.R. Schoeberl, and J.J. Barnett, Monthly mean global climatology of temperature, wind, geopotential height and pressure for 0-120 km, *National Aeronautics and Space Administration*, Technical Memorandum 100697, Washington, D.C., 1988.
- Frey, R. A., B. A. Baum, W. P. Menzel, S. A. Ackerman, and C. C. Moeller. A comparison of cloud top heights computed from airborne lidar and mas radiance data using CO2-slicing. *J. Geophys. Res.*, **104**:24547–24555, 1999.
- Fu, R., et al., Short circuit of water vapor and polluted air to the global stratosphere by convective transport over the Tibetan Plateau. 5664–5669 PNAS, vol. **103**, no. 15, 2006.
- Geerts, B., G.M. Heymsfield, L. Tian, J.B. Halverson, A. Guillory and M.I. Mejia, Hurricane Georges’s Landfall in the Dominican Republic: Detailed Airborne Doppler Radar Imagery, *Bull. Am. Meteorol. Soc.*, **81**, 999-1018, 2000.
- Harris, A., Manning, E. M., Friedman, S. Z., AIRS Version 4.0 Released Files Description, JPL document D-31502, 2005.
- Hansen, J.E., Multiple scattering of polarized light in planetary atmospheres. Part II. Sunlight reflected by terrestrial water clouds, *J. Atmos. Sci.*, **28**, p1400, 1971.

- Heymsfield, A. J., and L. J. Donner, A scheme for parameterizing ice-cloud water in general circulation models, *J. Atmos. Sci.*, **47**, 1865-1877, 1990.
- Heymsfield, A. J., A. Bansemer, P. R. Field, S. L. Durden, J. L. Stith, J. E. Dye, W. Hall, and C. A. Grainger: Observations and parameterizations of particle size distributions in deep tropical cirrus and stratiform precipitating clouds: Results from in situ observations in TRMM field campaigns. *J. Atmos. Sci.*, **59**, 3457-3491, 2002.
- Hogan, R. J., and A. J. Illingworth, Parameterizing ice cloud inhomogeneity and the overlap of inhomogeneities using cloud radar data. *J. Atmos. Sci.*, **60**, 756-767, 2003.
- Hogan, R. J., A. J. Illingworth, E. J. O'Connor, and J. P. V. Poilares Baptista, Characteristics of mixed-phase clouds. Part II: A climatology from ground-based lidar, *Q. J. R. Meteorol. Soc.*, **129**, 1-18, 2003.
- Houghton, J. T., et al., *Climate Change 2001: The Scientific Basis*. Cambridge University Press, 944p., 2001.
- Houze, Jr., R. A., S. S. Chen, D. E. Kingsmill, Y. Serra, and S. E. Yuter, Convection over the Pacific Warm Pool in relation to the atmospheric Kelvin-Rossby wave. *J. Atmos. Sci.*, **57**, 3058-3089, 2000.
- Intrieri, J. M., G. L. Stephens, W. L. Eberhard, and T. Uttal, A Method for Determining Cirrus Cloud Particle Sizes Using Lidar and Radar Backscatter Technique, *J. Appl., Meteor.*, **36**, No. 6, pp1074-1082, 1993.
- Jarnot, R.F., V.S. Perun, and M.J. Schwartz, Radiometric and spectral performance and calibration of the GHz bands of EOS MLS, *IEEE Trans. Geosci. Remote Sensing* **44**, no. **5**, 1131-1143, May 2006.
- Jiang, Y. B., et al., Validation of the Aura Microwave Limb Sounder Ozone by Ozonesonde and Lidar Measurements, *J. Geophys. Res.* This issue, 2007.
- Joiner, J., and A. P. Vasilkov, First results from the OMI Rotational Raman scattering cloud pressure algorithm, *IEEE Trans. Geosci. Remote Sens.*, **44**, no. 5, 1272-1282, 2006.
- Kahn, B. H., A. Eldering, A. J. Braverman, E. J. Fetzer, J. H. Jiang, E. Fishbein, and D. L. Wu, Toward the characterization of upper tropospheric clouds using Atmospheric Infrared Sounder and Microwave Limb Sounder observations, *J. Geophys. Res.*, **112**, D05202, doi:10.1029/2006JD007336, 2007.
- Korolev, A. V., G. A. Isaac, I. P. Mazin, and H. W. Barker, Microphysical properties of continental clouds from *in situ* measurements, *Q. J. R. Meteorol. Soc.*, **127**, 2117-2151, 2001.
- Lary, D. J., and L. Lait, Using probability distribution functions for satellite validation, *IEEE Trans. Geosci. Remote Sens.*, **44**, no. **5**, 1359-1366, 2006.
- Li, J.-L., et al., Comparisons of EOS MLS Cloud Ice Measurements with ECMWF analyses and GCM Simulations: Initial Results, *Geophys. Res. Lett.* **32**, L18710, doi:10.1029/2005GL023788, 2005.
- Li, J.-L., J.H. Jiang, D.E. Waliser, and A.M. Tompkins, Assessing Consistency between EOS MLS and ECMWF Analyzed and Forecast Estimates of Cloud Ice, *Geophys. Res. Lett.*, in review. 2007.
- Li, Q. B., et al., Convective outflow of South Asian pollution: A global CTM simulation compared with EOS MLS observations, *Geophys. Res. Lett.* **32**, no. **14**, L14826, doi:10.1029/2005GL022762, 2005.
- Liu, G., and J. A. Curry, Determination of ice water path and mass median particle size using multichannel microwave measurements, *J. Appl. Meteorol.*, **39**, 1318-1329, 2000.
- Livesey, N.J., W.V. Snyder, W.G. Read, and P.A. Wagner, Retrieval algorithms for the EOS

- Microwave Limb Sounder (MLS) instrument, *IEEE Trans. Geosci. Remote Sensing* **44**, no. **5**, 1144-1155, May 2006.
- Livesey, N. J., et al., Validation of eos microwave limb sounder o3 and co observations in the upper tropospheric and lower stratospheric, *J. Geophys. Res.*, this issue, 2007.
- 5 Mace, G. G., E. E. Clouthiaux, and T. P. Ackerman, The composite characteristics of cirrus clouds: Bulk properties revealed by one year of continuous cloud radar data. *J. Climate*, **14**, 2185-2203, 2001.
- Mahfouf, J.-F., Influence of physical processes on the tangent-linear approximation, *Tellus.*, **51**, 147-166, 1999.
- 10 Matrosov, S. Y., et al., Retrieval of vertical profiles of cirrus cloud microphysical parameters from Doppler radar and infrared radiometer measurements. *J. Appl. Meteor.*, **33**, 617-626, 1994.
- Matrosov, S. Y., A. V. Korolev, and A. J. Heymsfield, Profiling cloud mass and particle characteristic size from Doppler radar measurements, *J. Atmos. Oceanic Technol.*, **19**, 1003-1018, 2002.
- 15 McFarquhar, G. M., and A. J. Heymsfield, Microphysical characteristics of three anvils sampled during the central equatorial pacific experiment. *J. Atmos. Sci.*, **53**, 2401-2423, 1996.
- McFarquhar, G. M., and A. J. Heymsfield, Parameterization of tropical cirrus ice crystal size distributions and implications for radiative transfer: Results from CEPEX. *J. Atmos. Sci.*, **54**, 2187-2200, 1997.
- 20 Oslen E. T. (eds.), Granger S., Fetzer, E. Fishbein, E. Manning, L. Iredell, AIRS/AMSU/HSB version 4.0 Level 3 quick start, Version 4.3 L3 QA Quick Start Documentation, 2005.
- Pardo, J. R., E. Serabyn, and J. Cernicharo, Submillimeter atmospheric transmission measurements on Mauna Kea during extremely dry El Nino conditions: Implications for broadband opacity contributions. *J.Q.S.R.T.*, **67**, 169-180, 2000.
- 25 Pickett, H.M., Microwave Limb Sounder THz Module on Aura, *IEEE Trans. Geosci. Remote Sensing* **44**, no. 5, 1122-1130, May 2006.
- Platt, C. M. R., A parameterization of the visible extinction coefficient in terms of the ice/water content. *J. Atmos. Sci.*, **48**, 2083-2098, 1997.
- Read, W. G., Z. Shippony, M.J. Schwartz, N.J. Livesey, and W.V. Snyder, The clear-sky unpolarized forward model for the EOS Microwave Limb Sounder (MLS), *IEEE Trans. Geosci. Remote Sensing* **44**, no. **5**, 1367-1379, 2006.
- 30 Read, W. G., et al., Eos aura microwave limb sounder upper tropospheric and lower stratospheric humidity validation, *J. Geophys. Res.*, this issue, 2007.
- Santee et al., Validation of Aura Microwave Limb Sounder HNO₃ Measurements, *J. Geophys. Res.*, this issue, 2007.
- 35 Schwartz, et al., Validation of the Aura Microwave Limb Sounder (MLS) temperature and geopotential height measurements, This issue, 2007.
- Skofronick-Jackson, G. M., and J. R. Wang, The estimation of hydrometeor profiles from wideband microwave observations. *J. Appl. Meteor.*, **39**, 1645-1656, 2000.
- 40 Stephens, G.L., S.C. Tsay, P.W. Stackhouse., P.J. Flatau, The relevance of the microphysical and radiative properties of cirrus clouds to climate and climatic feedback, *J. Atmos. Sci.*, **47**, p1742., 1990.
- Stephens, G. L., and Coauthors, The CloudSat mission and the EOS constellation: A new dimension of space-based observations of clouds and precipitation. *Bull. Amer. Meteor. Soc.*, **83**, 1771-1790, 2002.
- 45 Su, H., W.G. Read, J.H. Jiang, J.W. Waters, D.L. Wu, and E.J. Fetzer, "Enhanced positive water

- vapor feedback associated with tropical deep convection: New evidence from Aura MLS," *Geophys. Res. Lett.* **33**, L05709, doi:10.1029/2005GL025505, 2006.
- Vivekanandan, J., J. Turk, and V. N. Bringi, Ice water path estimation and characterization using passive microwave radiometry. *J. Appl. Meteor.*, **30**, 1407-1421, 1991.
- 5 Waters, J. W., Microwave limb sounding. *Atmospheric Remote Sensing by Microwave Radiometry*. M. A. Janssen, Ed., John Wiley and Sons, Inc., 572 pp., 1993.
- Waters, J.W., et al., The Earth Observing System Microwave Limb Sounder (EOS MLS) on the Aura satellite, *IEEE Trans. Geosci. Remote Sensing* **44**, no. **5**, 1075-1092, May 2006.
- Weng, F., and N. C. Grody, Retrieval of ice cloud parameters using a microwave imaging
10 radiometer. *J. Atmos. Sci.*, **57**, 1069-1081, 2000.
- Wilheit, T. T., et al., Microwave radiometric observations near 19.35, 95 and 183 GHz of precipitation in tropical storm Cora, *J. Appl., Meteorol.*, **21**, 1137-1145, 1982.
- Wu, D. L., and J. H. Jiang, EOS MLS Algorithm Theoretical Basis for Cloud Measurements, JPL Document-19299, 2004.
- 15 Wu, D. L., W. G. Read, A. E. Dessler, S. C. Sherwood, and J. H. Jiang, UARS MLS Cloud Ice Measurements and Implications for H₂O Transport near the Tropopause, *J. Atmos. Sci.*, **62** (2): 518-530, 2005.
- Wu, D.L., J.H. Jiang, and C.P. Davis, EOS MLS cloud ice measurements and cloudy-sky radiative transfer model, *IEEE Trans. Geosci. Remote Sensing* **44**, no. **5**, 1156-1165, May 2006.
- 20 Yeh, H.-Y. M., N. Prasad, R. A. Mack, and R. F. Adler, Aircraft microwave observation and simulations of deep convection from 8 to 183 GHz, Part I: Model results. *J. Atmos. Oceanic Tech.*, **7**, 392-410, 1990.

7 Appendices

7.1 Appendix A: MLS V2.2 Level 2 Processing

Like MLS V1.5 algorithm [Livesey et al., 2006], the v2.2 software processes MLS radiance measurements through multiple phases. The cloud detection and the retrieved atmospheric state are improved together as the retrieval progresses in phase.

Fig.A1 illustrates the V2.2 data processing flow where cloud flags are updated several times as the retrieval progresses through its phases. The V2.2 cloud flags are based on T_{cir} estimated at the end of the earlier phase for R1, R2 and R4. Different fundamentally from V1.5 in R3 cloud detection, the V2.2 algorithm detects clouds based on the χ^2 of the fitted radiance residuals near the 233.9 GHz $O^{18}O$ line (Band 8). The modeled clear-sky radiances are updated at the end of each retrieval phase from the newly retrieved atmospheric state. Atmospheric variables most important for determining T_{cir} are temperature (T), tangent pressure (P_{tan}), H_2O , O_3 , HNO_3 profiles.

As shown in Fig.A1, the V2.2 retrieval phases contain *Core* (*InitPtan*, *InitR2*, *UpdatePtan*, *InitExt*, *FinalExt*, *FinalPtan*, *InitRHi* and *InitUTH*), *Core+R3*, *Core+R2*, *HighCloud*, *Core+R4* (A and B), and *Core+R5*. The *Core* phase is aimed to obtain a reliable initial atmospheric state through several sub-phases. The first two sub-phases, *InitPtan* and *InitR2*, are structured to obtain an initial estimate of atmospheric variables in the stratosphere, which use only radiances above cloud altitudes to avoid potential impacts from clouds. At the end these phases T_{cir} 's are estimated for the R1 radiances using the retrieved T , P_{tan} and other *a priori* profiles extended into the troposphere. The R1 radiances exceeding the cloud thresholds in Table A1 are flagged, and the flagged radiances are excluded in *UpdatePtan*, a subsequent phase to retrieve T and P_{tan} once again by including the R1 radiances at the tropospheric tangent heights.

The rest sub-phases in *Core* are configured to refine T and P_{tan} retrievals with a better vertical resolution and include the R2 radiances to obtain a good initial guess for the H₂O in the UT/LS region. Before using the R3 radiances, the V2.2 algorithm first retrieves a background total extinction profile using the window channel at 240 GHz, which accounts for most of the spectrally flat component in the R3 radiances. This retrieval is divided to two sub-phases, *InitExt* and *FinalExt*, to deal with potential cloud effects. The *InitExt* phase uses R3 window-channel radiances only at $P_{tan} < 250$ hPa so that the extinction retrieval is always converged in cloudy cases. The *FinalExt* phase is designed to further update the extinction profile retrieved in *InitExt* by using all the window-channel and Band 8 radiances down to the surface. However, the update may not occur in a bad cloudy case, and the extinction retrieval from *FinalExt* will relax to the *InitExt* profile if this happens. Large (>30) Band-8 χ^2 from *FinalExt* are used to flag R3 radiances on a MIF-by-MIF basis. The flagged R3 radiances are excluded in the *FinalP_{tan}* phase that is configured to finalize T and P_{tan} retrievals using both R1 and R3 radiances.

After the T and P_{tan} retrievals are completed, the last two sub-phases in *Core* are introduced to provide an initial guess for H₂O in the UT/LS region using R2 radiances, with *InitRHi* featuring the mid-tropospheric RHi and *InitUTH* featuring the UT/LS H₂O. No cloud flags are imposed for these retrievals, and the configured algorithms rely on their own skills to handle cloud impacts. For example, the RHi from *InitRHi* is capped at 110%; whereas *InitUTH* uses only R2 radiances at $P_{tan} < 350$ hPa and retrieves radiance baselines along with H₂O profile. Improved from V1.5, such a configuration performs well in dealing with cloudy cases and yields a reasonably good initial guess for the final H₂O retrieval in the next phase. Using the initial guess of H₂O, R1 and R2 T_{cir} 's are calculated at the end of *Core*.

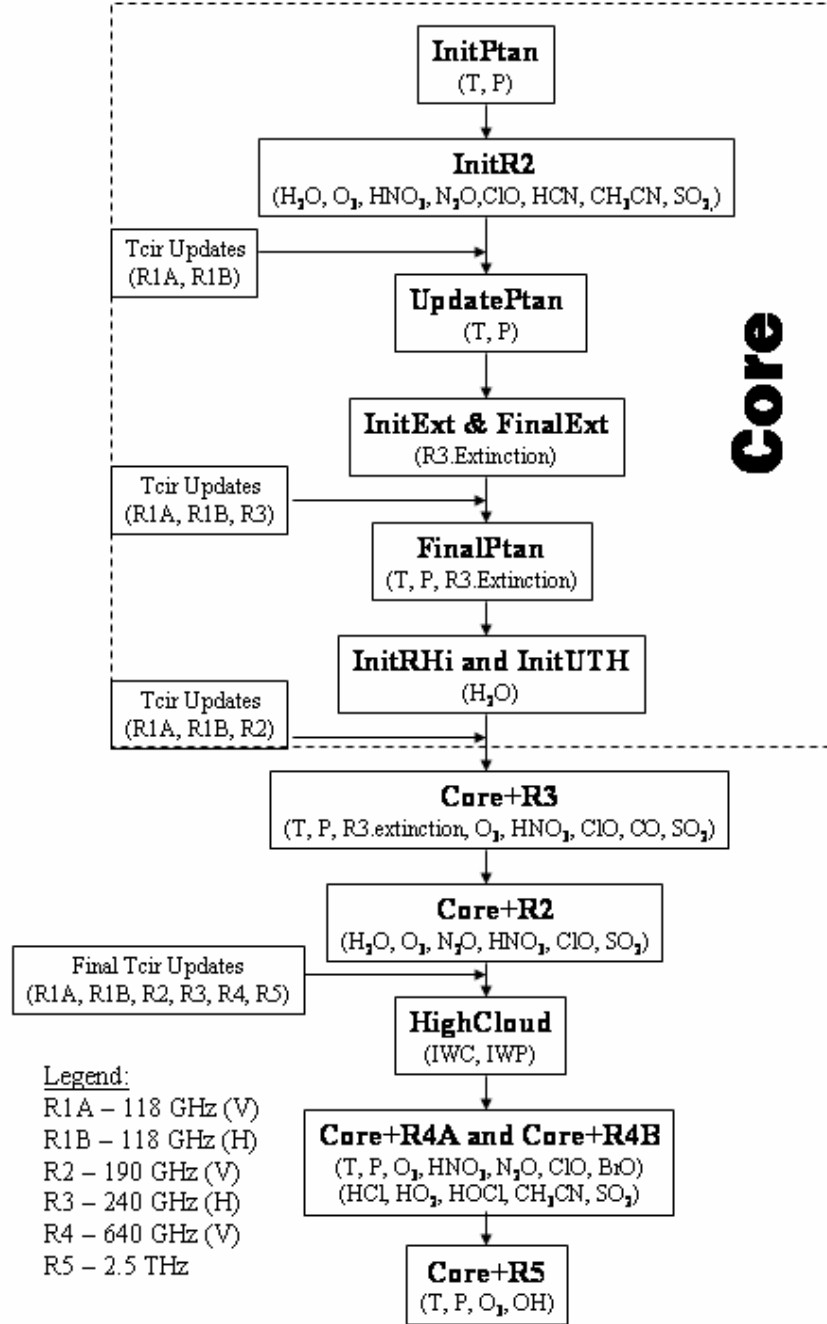


Figure A1. Data flow diagram of MLS V2.2 Level 2 processing. The atmospheric variables retrieved in each phase are listed in the parenthesis. *Tcir* is updated three times in the *Core* phase to ensure stable retrievals of clear-sky gaseous species. MLS radiometers and their associated frequencies are given in the legend.

- 5 The phases after *Core* are essentially parallel to each other. Flagged radiances are excluded in *Core+R3* and *Core+R2* retrievals. The cloud ice retrieval, *HighCloud*, is placed after *Core+R3* and *Core+R2*, because the best *Tcir* estimate comes after *T*, *Ptan*, *H₂O*, *O₃*, and *HNO₃* retrievals are

finalized. The final T_{cir} 's for all radiometers are obtained in the *HighCloud* phase and averaged into the standard vertical pressure levels (12 levels per decade), which go to the cloud IWC and IWP retrievals. Additional frequency averaging is applied to R4 T_{cir} to further reduce radiance measurement noise. Neither *Core+R4* nor *Core+R5* uses the cloud flags for radiance discrimination.

Table A1 MLS frequency channels and thresholds for cloud flag

Radiometer	Cloud Channel Frequency (GHz)	Low Threshold	High Threshold
R1A/R1B	B32.C4/B34.C4	$T_{cir} < -4$ K	none
118 GHz	115.3		
R2	B5.C1	$T_{cir} < -20$ K	$T_{cir} > 10$ K
190 GHz	178.8 and 204.9		
R3	B8	none	$\chi^2 > 30$
240 GHz	233.4-234.5 and 244.8-245.9		
R4	B11.C23	$T_{cir} < -10$ K	$T_{cir} > 10$ K
640 GHz	635.9 and 649.8		

7.2 Appendix B: Cloud Profiles and Equivalent Limb Length for Average IWC

a) Layered clouds

In the RT calculations with a 2-km layered cloud, we specify the cloud with a trapezoid profile

5 with i.e.,

$$w(z - z_c) = \begin{cases} 0 & z - z_c > 1 \\ 2(1 - z + z_c) & 1 > z - z_c > 0.5 \\ 1 & 0.5 > z - z_c > -0.5 \\ 2(1 + z - z_c) & -0.5 > z - z_c > -1 \\ 0 & z - z_c < -0.5 \end{cases}$$

where z_c is the center of the cloud layer, and $IWC(z) = IWC_0 \cdot w(z - z_c)$. Hence, at tangent height $h_t = z_c$, we have

$$10 \quad hIWP = 2 \int_{z_c}^{\infty} IWC(z) dz = 2 IWC_0 \int_{z_c}^{\infty} w(z) dz = IWC_0 \cdot L$$

where $L = 192$ km is the equivalent path length for a cloud with average IWC_0 . As a result, for the limb radiance at $h_t = z_c$, if $hIWP$ is small, T_{cir} is proportional to $hIWP$ and to the averaged IWC of the cloud layer with an equivalent path length of ~ 200 km.

b) Clouds with Exponentially-Decreasing IWC

15 In the case $IWC \propto e^{-z/H_0}$, we have

$$\begin{aligned}
hIWP &= 2IWC_0 \int_{h_t}^{\infty} e^{-z/H_0} ds \\
&= 2IWC_0 \int_{h_t}^{\infty} e^{-z/H_0} \frac{R_e + z}{\sqrt{(R_e + z)^2 - (R_e + h_t)^2}} dz \\
&\approx 2IWC_0 e^{-h_t/H_0} \int_0^{\infty} e^{-z/H_0} \frac{R_e}{\sqrt{2R_e z}} dz \\
&\approx IWC(h_t) \sqrt{2R_e H_0} \Gamma(0.5)
\end{aligned}$$

where R_e is the Earth's radius in km, H_0 is the scale height of decreasing IWC profile in km, and Gamma function $\Gamma(0.5)$ is 1.77. For small $hIWP$, we still obtain a relation that $Tcir$ is proportional to IWC at the pointing tangent height. In this case, the equivalent path length

5 $L = \sqrt{2R_e H_0} \Gamma(0.5) \approx 200\sqrt{H_0}$ in km. As suggested by the observed IWC climatology in the upper troposphere, H_0 varies typically between 1 and 2 km. For $H_0=1$ km, $L = \sim 200$ km; for $H_0=2$ km, $L = \sim 280$ km.

The distribution $IWC \propto e^{-z/H_0}$ also shifts contribution functions to a low altitude if the limb radiance has a finite beamwidth. MLS 240-GHz receiver has a Gaussian beam pattern with 3.2 km

10 half-power beamwidth (HPBW), i.e., $e^{-(z-h_t)^2/2w^2}$, where $w=0.425 \cdot \text{HPBW}$. Unlike the WFs in Figure 4, which are centered at tangent height h_t , the contribution after convolving with $IWC \propto e^{-z/H_0}$ will shift down by w^2/H_0 . If HPBW=3.2 km, the shift will be 1.8 km for $H_0=1$ km and 0.9 km for $H_0=2$ km. In other words, we need to increase the width of vertical resolution from 3.2 km to 5 km for $H_0=1$ km and 4.1 km for $H_0=2$ km to embrace most of the contribution from

15 profiles like $IWC \propto e^{-z/H_0}$.